

A Structural and Dynamical Study of Late-Type, Edge-On Galaxies: I. Sample Selection and Imaging Data

Julianne J. Dalcanton¹

Department of Astronomy, University of Washington, Box 351850, Seattle WA, 98195
&

Observatories of the Carnegie Institution of Washington, 813 Santa Barbara Street,
Pasadena CA, 91101

Rebecca Bernstein^{2,3}

Observatories of the Carnegie Institution of Washington, 813 Santa Barbara Street,
Pasadena CA, 91101

ABSTRACT

We present optical (B & R) and infrared (K_s) images and photometry for a sample of 49 extremely late-type, edge-on disk galaxies selected from the Flat Galaxy Catalog of Karenchentsev et al. (1993). Our sample was selected to include galaxies with particularly large axial ratios, increasing the likelihood that the galaxies in the sample are truly edge-on. We have also concentrated the sample on galaxies with low apparent surface brightness, in order to increase the representation of intrinsically low surface brightness galaxies. Finally, the sample was chosen to have no apparent bulges or optical warps so that the galaxies represent undisturbed, “pure disk” systems. The resulting sample forms the basis for a much larger spectroscopic study designed to place constraints on the physical quantities and processes which shape disk galaxies.

The imaging data presented in this paper has been painstakingly reduced and calibrated to allow accurate surface photometry of features as faint as 30 mag/arcsec² in B and 29 mag/arcsec² in R on scales larger than 10". Due to limitations in sky subtraction and flat fielding, the infrared data can reach only to 22.5 mag/arcsec² in K_s on comparable scales. As part of this work, we have developed a new method for quantifying the reliability of surface photometry, which provides useful diagnostics for the presence of scattered light, optical emission from infrared cirrus, and other sources of non-uniform sky backgrounds.

¹e-mail address: jd@astro.washington.edu

²e-mail address: rab@ociw.edu

³Hubble Fellow

Subject headings: galaxies: formation — galaxies: fundamental parameters — galaxies: irregular — galaxies: spiral — galaxies: structure

1. Introduction

Basic physics must be responsible for final differentiation of galactic structure. Mass, angular momentum, density, environment, and metallicity all must contribute to the shape and relative proportions of the disk and spheroid structures observed today. While the tremendous diversity of the galaxy population suggests a bewildering level of complexity in the *details* of galaxy formation, the existence of broad patterns, such as the Fundamental Plane or the Tully-Fisher relation, gives some hope that the overall structure of galaxies are controlled by large scale physics, and thus can be explained and constrained with observation.

Disk galaxies represent some of the best possible laboratories for exploring the physics which controls galaxy formation. Spiral disks are less corrupted by dissipation and angular momentum transport than comparable elliptical galaxies, and thus they better preserve the initial conditions from which they were formed. Likewise, the disks of spiral galaxies extend far out into their dark matter halos, and thus can be used to probe the shape and extent of the accompanying dark matter, which in turn places strong constraints on theories of dark matter and structure formation. Finally, only in spirals can we directly observe galaxy formation *in process*, particularly among late type spiral disks and low surface brightness galaxies, which, from their colors, IR surface brightnesses, and gas content, seem to be forming stars for nearly the first time.

To place observational constraints upon the process of galaxy formation, we have begun a comprehensive program to study the dynamics, gas content, metallicity, and stellar populations of a sample of late-type, bulgeless disk galaxies. This population forms a structurally uniform sample, allowing us to isolate changes in the physical properties of the galaxies (i.e. mass, angular momentum, etc.) independent of changes in morphology. By avoiding systems with bulges, we also limit the degree to which the baryonic component of the galaxy may have been affected by dissipation or angular momentum transport during formation.

We have selected these galaxies from a large catalog of edge-on galaxies, described below in §2. By selecting the galaxies edge-on, we can ensure that the galaxies are free of strong warps, which could indicate a recent interaction or a non-equilibrium configuration.

The galaxies in our sample should therefore be well relaxed and largely undisturbed. Furthermore, while the edge-on view of a galaxy can clearly identify it as a disk, it disguises the face-on morphology, masking the presence or absence of spiral arms, bars, or star formation regions. Thus, the selection of an edge-on sample should be unbiased with respect to these transient features. Finally, the edge-on orientation of these galaxies allows direct study of their vertical structure. The vertical structure of galactic disks contains information on the balance between the surface density of the disk, the vertical velocity dispersion of the stars, and the density structure of the halo. Thus this sample will provide constraints (albeit highly interdependent constraints) on the internal dynamics of the disk and the flattening of the halo (Spitzer 1942, van der Kruit & Searle 1982, Bahcall 1984, Zasov et al. 1991, Dove & Thronson 1993, Olling 1995, van der Kruit & de Grijs 1999).

Most importantly, by selecting galaxies edge-on, we allow ourselves to sample a wider range of disk surface brightnesses. Low surface brightness galaxies tend to have low internal extinction (de Blok & van der Hulst 1998, McGaugh 1994), and thus there is a substantial enhancement in their apparent surface brightness when viewed edge-on. Selecting edge-on galaxies therefore admits galaxies which would otherwise be too low surface brightness to detect or to study (particularly in the infrared). As the dynamics of low surface brightness galaxies tend to be dominated by the dark matter halo (Swaters et al. 2000, de Blok & McGaugh 1997; although see van den Bosch et al. 2000), these systems make ideal probes of the halo’s density structure.

Observationally, we are studying these galaxies through a combination of optical and infrared imaging (to constrain the mass of the stellar disk and the structure of the galaxy, and to roughly limit the current stellar populations and dust content), high-resolution long-slit spectroscopy of the $H\alpha$ line and nearby [NII] and [SII] doublets (to study the internal dynamics of the disk and limit the abundance of the gas phase), low-resolution spectroscopy of the region between $H\beta$ and $H\alpha$ (to map internal extinction across the disk), and HI observations (to constrain the total mass and distribution of atomic gas in the disk). In this first paper, we present the sample, the imaging data, and the resulting photometry, with a complete analysis of the errors and uncertainties. We delay a full analysis of the galaxy colors and structural properties until a later paper in the series.

2. Sample Selection

The sample was selected from the Flat Galaxy Catalog (FGC) of Karachentsev et al. (1993), a catalog of 4455 edge-on galaxies with axial ratios greater than 7, and major axis lengths of $> 0.6'$. The FGC was originally selected by visual inspection of the O POSS

plates in the north ($\delta > -27$ deg) and the J films of the ESO/SERC survey in the south ($\delta < -17$ deg). Galaxies from the ESO plates are known as the FGCE, and have slightly different properties due to small differences in the plate material. From the combined FGC/FGCE catalog, we selected galaxies which appeared both bulgeless and low surface brightness on the Digitized Sky Survey (DSS), and which showed no signs of inclination (major-to-minor axis ratio $a/b > 8$) or interaction. Unfortunately, our selection criteria were not uniformly successful, as the images in §7 and Figure 3 will show. Due to the low resolution of the DSS, $\lesssim 10\%$ of the galaxies which met the original selection criteria showed small bulges which were not apparent on the DSS, or dust lanes which masked a high-surface brightness disk (e.g. FGC 446, FGC 1043, FGC 1440, & FGC E1371). As these galaxies will be useful for some aspects of our extended scientific program, we have retained them in the sample, but treated them separately when appropriate. One galaxy which we had originally chosen for the survey, FGC E1550, showed a pronounced integral-sign-shaped warp in our initial R band imaging, and was removed from the sample. The final sample is listed in Table 1 along with positions and orientations as given in the FGC.

The resulting distribution of morphological types and surface brightness classes (I=high surface brightness, IV=low surface brightness), both as given by the FGC, are plotted in Figure 1, along with the distributions for the entire FGC catalog. Clearly our sample is biased towards later types and lower surface brightnesses than the FGC as a whole. We have also plotted the distributions of blue axial ratios for our sample in Figure 2. Our subsample has a higher mean axial ratio than the catalog as a whole, betraying our selection bias for the most nearly edge-on galaxies. It may also reflect our choice of late morphological types; an analysis of the FGC by Kudrya et al. (1994) shows that the galaxies in the FGC become progressively thinner with later Hubble types, with the limiting axial ratio varying from $(a/b)_{max} = 14.1$ for Sb galaxies to $(a/b)_{max} = 27.0$ for Sd's. This trend towards intrinsically thinner galaxies with increasing Hubble type is also seen by de Grijs (1998). The apparent bias towards large axial ratios may also result from our selection of lower surface brightness galaxies. LSBs are known to have larger disk scale lengths than normal galaxies with similar rotation speeds (Zwaan et al 1995), and consequently may have larger axial ratios as well.

Many of the galaxies in our sample were previously observed in single dish HI observations with Arecibo. For our $8h < RA < 19h$ sample (spring observing season), we concentrated on those galaxies which had HI detections and which were relatively nearby ($V \lesssim 5000$ km/s), giving us better spatial resolution for both imaging and spectroscopy. During the fall, slightly more than half (18 of 32) of our sample galaxies had existing HI observations. Overall, 75% of the galaxies in our survey have published single dish HI observations. When available, the heliocentric velocity and the corrected line width at 50% peak flux ($W_{50,c}$) are listed in Table 1. The majority of these are from a large survey of

FGC galaxies observed at Arecibo by Giovanelli et al. (1997). These are supplemented with measurements for FGC 164 from Schneider et al. (1990), and for FGC 349 from Haynes et al. (1997).

In addition to HI observations, a very small number of the galaxies in our sample (FGC 446, FGC 1043, and FGC 2217) were detected as part of the IRAS Faint Source Catalog (Moshir et al. 1990; F03422+0544, F10131+0734, 18356+1729 respectively). In order of increasing 60μ flux, FGC 1043 is detected in both 60μ and 100μ bands, with flux of 0.23 Jy and 0.65 Jy, respectively; FGC 446 is only detected at 60μ , with flux of 0.38 Jy; and FGC 2217 is detected at 25μ and 60μ , with flux of 0.17 Jy and 1.25 Jy, respectively. All of the detections and upper limits are consistent with spectra which rise in νf_ν towards 100μ .

While our sample galaxies are exceptionally useful probes of the properties of galaxies over a spectrum of mass and surface brightness, they by no means constitute a statistical sample of any sort. They are not drawn randomly from the FGC, and thus their properties are not representative of that catalog as a whole. Because our selection of a subsample was far from unbiased, the sample cannot be used for any analysis of the numbers of galaxies of different surface brightnesses. Likewise, the sample cannot be used to study the incidence of warping at moderately bright surface brightness levels.

Finally, our subsample of the FGC includes galaxies with peak B -band surface brightnesses (viewed edge-on) between 21.5 and 23 mag/arcsec² – i.e. between the face-on value of the characteristic Freeman (1970) surface brightness and the surface brightness limit of the FGC survey data. Thus, this limited range of B -band surface brightness can become a selection effect which can influence some results, such as apparent trends in color and extinction. These biases will be considered explicitly.

3. Optical Observations, Data Reduction, & Photometric Calibration

3.1. Optical Imaging

All optical observations of the FGC sample were made with the 2.5 meter Dupont telescope on Las Campanas, during the nights of September 22 and 23 in 1997, and March 29 and 30 in 1998, using a thinned Tektronix 2048² CCD (“Tek5”) with 0.259” pixels, a gain of ~ 2.4 DN/ e^- , and readnoise of $\sim 7e^-$. The conditions were photometric for the duration of all four nights. For each galaxy, a series of three exposures was taken through both a Johnson B and a Kron-Cousins R filter, with the position of the telescope shifted by more than 2’ between exposures to minimize large and small scale flat-fielding variations, cosmic rays, and cosmetic defects on the CCD. Typical exposure times for the fall subsample were

300 seconds per frame in B , and 120 seconds per frame in R , for combined exposure times of 15 minutes and 6 minutes respectively. In order to maximize our chances of detecting extended stellar halos in the nearby spring sample, our exposure times for the spring sample were 2–3 times longer.

While the March 1998 observations were made during new moon, the September 1997 observations were made with 40-50% moon illumination for the second half of each night. During the night of September 23, 1997, time limitations forced us to image FGC 164, FGC 215, FGC 225, FGC 256, FGC 349, FGC 436, FGC 442 and FGC 446 while the moon was up; as a result of the increased sky brightness, the B images of these galaxies are noticeably shallower. Typical sky brightnesses without moon were 22.2 ± 0.2 mag/arcsec² and 20.6 ± 0.2 mag/arcsec² in B and R respectively, and 21.5 ± 0.5 mag/arcsec² and 19.9 ± 0.5 mag/arcsec² after the moon had risen fully. The total exposure times, sky brightnesses, seeing FWHMs, and fluctuation levels of the reduced images are listed in Table 2.

3.2. Image Reduction

Each raw image has a bias level consisting of a time-variable mean which changes by ± 1 DN between images and causes ± 0.5 DN vertical structure along columns. There is also a stable component, which is a small exponential decay over the first 150 pixels in every row. The time-variable bias level can be identified in the 30 columns of overscan taken in each image. To remove it, we fit the average of these columns with a 10th order polynomial and subtracted this fit column by column. A bias image was then made by averaging 15-20 overscan-subtracted, zero second exposures, with 2 iterations of $\pm 3\sigma$ rejection to remove cosmic rays. This image is then smoothed with a 1x4 boxcar to reduce pixel-to-pixel noise to ± 0.3 DN, and then subtracted from each image to remove the stable exponential structure. Dark frames show that the dark current in the CCD is less than 0.5 DN per 900sec exposure with no two-dimensional structure evident. No dark correction was therefore applied.

Pixel-to-pixel flat fields were generated separately for each night using dome flats. The resulting flat fields were divided into all bias subtracted images, including twilight flats. Except for large-scale illumination changes due to the relative changes in the telescope and dome positioning, differences between the dome flats on adjacent nights were less than 0.3%, peak-to-peak. To enable faint surface photometry over reasonably large areas (1–2'), we have taken particular care with the large scale flat-field calibration of our images. To remove large-scale illumination features and to correct for the difference in color between the night sky and the dome flats, twilight sky flats and night sky flats were created. The

B- and R-band twilight sky flats contained over 100,000 counts, cumulative.

The night sky flats were made by averaging the science exposures after rescaling them to a common exposure time (multiplicative) and mean sky level (additive) and using IRAF’s CCDCLIP rejection with a grow radius of 10-30 pixels to eliminate stars, galaxies, and cosmic rays; roughly 30 images per night were used in this average. As the object galaxies were moved by several arcminutes between exposures, the target objects were rejected cleanly, and roughly 75% of the images could usefully contribute to the flat field in any region of the CCD. We then median smoothed the combined images on a $\sim 2''$ scale to reduce the pixel-to-pixel noise to ~ 0.001 DN (~ 28 mag/arcsec² for a sky level of 20.5 mag/arcsec²), while preserving the large scale illumination correction. With the exception of one dust feature, the twilight and night sky flats had peak-to-peak amplitude of much less than 0.5% (corresponding to roughly 26.5 R mag/arcsec² or 28.3 B mag/arcsec²).

For the moonless portion of the September 1997 observations, the illumination was very uniform, and correction with twilight flats alone yielded images in which no repeating large scale structures were evident at the 0.5% level between the flat-fielded science images. Diffuse optical emission from galactic cirrus could clearly be detected in some of the lower latitude fields, immediately suggesting that flat-fielding residuals were small. High frequency structure (e.g. dust “donuts”) in the R -band twilight flat was isolated by dividing a heavily smoothed version (26'') of the flat into the original. This provided a high-frequency color correction to the dome flats, the maximum amplitude of which was $\lesssim 1\%$.

Because of the color change of the sky after moonrise, separate night sky flats were generated from and applied to the B - and R -band September 1997 observations taken after moonrise. Night sky flats were also applied to all of the March 1998 observations, for which the color and illumination of the twilights were not a good match to the night sky during science observations.

The images were aligned by matching SExtractor (Bertin & Arnouts 1996) positions for all objects in the R and B images. The resulting pairs were used to shift the images into accurate alignment with one of the R -band images, using IRAF’s GEOMAP and GEOTRANS packages. All images were then averaged together with $\pm 4\sigma$ rejection to produce the final images. To simplify later analysis, both B and R band images were rotated to orient the galaxy horizontally. The required rotation was identified by measuring the position of each galaxy at more than 4 locations along the disk in the R -band image. Finally, a 982x982 subsection was extracted from each image, centered on the galaxy.

3.3. Photometric Calibration

Photometric calibration for the optical observations was straightforward due to the nearly ideal conditions during the run. At least two separate Landolt (1983, 1992) standard fields were observed at the beginning and end of the night, at a variety of exposure times and at airmasses between 1.1 and 2.5. At least two more sets of standard observations were made during the course of each night, giving a total of 35-57 individual standard star measurements per night through each filter. The fluxes of the standard stars were measured within the $14''$ diameter aperture used by Landolt. For the Fall run, the photometric solution was made assuming a constant zero point and color term, with an airmass term allowed to vary night-to-night. For the Spring run, the zero point, color term, and airmass were allowed to vary each night; the resulting terms agreed to within $\pm 1\sigma$. Residuals from the best fit photometric solution were typically $\sigma_m = 0.012 - 0.020$. The resulting solutions are given in Table 3.

Few of the galaxies in our sample have been extensively observed in the optical. As a result, we have few means to check our calibration for consistency with other authors. One galaxy from our sample, FGC E1371, was also studied in the ESO-LV catalog (Lauberts & Valentijn 1989; eso-lv 3380010). The reported ESO-LV magnitudes are $B_{25}(\text{Cousins}) = 18.15 \pm 0.09$, $B_{26}(\text{Cousins}) = 17.95 \pm 0.09$, $R_{25}(\text{Cousins}) = 16.22 \pm 0.09$, and $R_{26}(\text{Cousins}) = 16.06 \pm 0.09$. In our filter system (Johnson B , Cousins R), we find $B_{25}(\text{Johnson}) = 18.27$, $B_{26}(\text{Johnson}) = 18.04$, $R_{25}(\text{Cousins}) = 16.23$, and $R_{26}(\text{Cousins}) = 16.21$, giving offsets of $+0.12$, $+0.09$, $+0.01$, and $+0.15$ from the ESO-LV measurements. These results are consistent within the errors (± 0.15 for our sample).

4. Infrared Observations, Data Reduction, & Photometric Calibration

4.1. Infrared Imaging

The infrared observations of the FGC sample were made with the duPont 2.5m telescope at Las Campanas Observatory, using an updated version of the IRCAM camera originally described in Persson et al. (1992), with the upgraded camera being similar to the P60IRC described by Murphy et al. (1995). The IRCAM, which consists of a Rockwell NICMOS3 256x256 HgCdTe chip with 40μ pixels, was operated at $f/7.5$ giving $0.348''$ pixels and an $89''$ field-of-view. All observations were made through the K_s filter (developed by M. Skrutskie and described in the Appendix of Persson et al. 1998), which cuts off at $\sim 2.2\mu$ to reduce the thermal background by a factor of two. All observations took place during three runs: 21-22 September 1997, 10-14 October 1997, and 13-14 April 1998. Observing

conditions on usable nights were as follows: September 21 & 22, photometric; October 10, clear for the first half of the night; October 11, photometric with high winds and poor seeing; October 14, photometric with very high winds and a 7.8 earthquake in the middle of the night; April 13, non-photometric; and April 14, photometric. The electronics for the camera were replaced between the Fall 1997 runs and the Spring 1998 run, changing the gain from 4.8 e-/adu to 7.5 e-/adu and requiring a new linearity correction.

Observations were made by looping the camera through successive sets of 6 exposures of 20 seconds (2 minutes total) at various positions, typically shifting the telescope by 1/2 of the camera field-of-view ($\sim 35 - 45''$) between exposure loops. Because of the thinness of the FGC, our mosaic pattern allowed at least part of the galaxy to be on the chip during every exposure, giving us high observing efficiency without affecting our ability to create sky frames. The shifts were in the direction which maximized the overlap between the chip and the galaxy (i.e. galaxies aligned East-West were dithered North-South). This strategy will limit our ability to reliably interpret faint infrared structures more than $20''$ above the planes of the galaxies. However, given the existence of low-level ghosting in the IRCAM and the faintness of the FGC subsample, such scientific inquiries are beyond the limits of the data, regardless.

Total exposure times varied widely for our galaxies. In keeping with the wide range in K_s band surface brightness, which spanned 4 mag/arcsec^2 , the most massive galaxies were well exposed in only 12 minutes of observations, while the lowest mass galaxies were still barely detectable after several hours of integration. Table 4 lists the UT dates of all our observations, along with the exposure times and estimates of the photometric quality (discussed in §4.2).

4.2. Image Reduction

Before processing, all images were linearized using scripts kindly supplied by S. E. Persson. (These scripts differed slightly between 1997 and 1998, due to the change in electronics.) The linearization was tested with data taken during the night of October 12 1997, while the dome was closed due to bad weather. For count levels less than 20,000 cts/pixel, the linearized data was linear to better than 0.1%; for reference, our typical sky levels in 20 second exposures were 6000 cts/pixel or less. The linearization procedure was not tested during the 1998 run.

All loops of exposures at a single position and exposure time were averaged together using $\pm 5\sigma$ rejection to remove cosmic rays. Dark frames were created each night

by combining loops of 50-100 exposures at every exposure time used for our science observations, and were subtracted from the appropriate images. On the night of April 14 1998, darks were taken in both the evening and morning, and were found to differ by $\sim 15\%$; no explanation for this variation was evident, and the two sets of darks were simply averaged together. The data from September 20 1997 were reduced using darks taken the following night.

Domeflats were derived most nights and divided into the summed, dark-subtracted images. Exceptions were the nights of October 10 and 11, for which domeflats taken during the night on October 12th were used. The domeflats from October 10 and 11 were obtained during the daytime with much warmer temperatures, and approached the level of non-linearity. Domeflats taken on the night of April 13 produced large scale illumination residuals relative to twilight flats taken on April 14. Domeflats taken on April 15 were used instead. (No domeflats were taken on April 14 because the calibrations lamps broke.) After dark subtraction and flattening, known bad pixels were replaced with locally interpolated values. Henceforth, we will use “images” to refer to these coadded, calibrated frames, and not the individual loop sub-exposures.

Sky subtraction and image alignment was performed with a modified version of the DIMSUM V2.0 package. First, a running sky image was created from the median of every 6 adjacent sets of co-added images, and then subtracted from the central image of the time series. At the beginning and end of each time series, no fewer than 4 adjacent images were used to create the sky image. Next, a rough offset was calculated using the centroid of a single star in each image, and then refined using IMALIGN with all stars available in the frame. These offsets were used to align the frames and then co-add them into a single image. The deep image was then used to create a mask of all objects. While the standard DIMSUM masking procedure works well for compact, reasonably well-exposed objects, it was necessary to modify DIMSUM’s masking procedure to create appropriate masks for the extended, low surface brightness galaxy in the frame. The masks were then de-registered, and used to create refined sky images for each frame. The new sky-subtracted images were then realigned and coadded to produce the final image. During the final alignment, the images were expanded by a factor of 4 to avoid loss of resolution when shifting the images. For images of standard stars, a sky image was created from all science exposures for the night and then scaled to the image median and subtracted. The resulting IR images were rotated and aligned with the optical R band images using IRAF’s GEOMAP and GEOTRANS packages. To reduce uncertainties in aligning a single image, after one pass through all of the data, the mean scale factor was derived for the transformation between K_s and R . The images were then realigned using the fixed scale factor.

While the seeing during our infrared run ($\sim 1.1''$) was not ideal, our final image resolution was also affected by the difficulty in aligning some of our images. Many of the galaxies were at sufficiently high galactic latitude that there were no bright stars visible in the individual images. As the galaxies themselves were often invisible in 120s exposures, and the duPont control software did not record pointing position until 1999, some of the co-added images were aligned using under-exposed faint stars, leading to non-spherical PSFs in the co-added frames. We were also troubled by high East-West windshake, compounding this problem. To account for this, we have fit all stars in our K_s images with elliptical Gaussian profiles. The PSF was measured for all available stars selected from R -band SExtractor catalogs (CLASS_STAR >0.9). The mean properties of the PSF were calculated using the brightest half of the stars (as measured in K_s), iteratively rejecting outliers at the $\pm 3\sigma$ level. In Table 4, we report the resulting mean FWHM along the major axis of the PSF ellipse, the axis ratio of the PSF ellipse, and the position angle of the ellipse, measured relative to the position angle of the galaxies. Thus, galaxies whose K_s PSFs have position angles less than $\pm 45^\circ$ will have worse seeing along the plane of the galaxy, than perpendicular to the plane. In general, due to the paucity of bright stars in our images, the higher order shape parameters for the PSF are not particularly well measured in most cases (given that they are based upon 2-5 faint stars). Values within parentheses are based upon only a single star, and entries marked with a "-" had no stellar objects within the frame.

For galaxies whose images were obtained over the course of 2 or more nights, we reduced the images for each night separately. The final image was a weighted sum of the images from separate nights.

4.3. Photometric Calibration

Calibration was performed using the faint standard star sequence established by Persson et al. (1998). Each standard star was moved through the four quadrants of the chip to reproduce differences between the four amplifiers. Sets of standards were observed at the beginning and end of each night, and usually 3-5 times during the course of the night. The fluxes of the standards were measured within $10''$ diameter apertures, as in Persson et al. (1998).

For the 1997 data, a single magnitude zero point and color term was found by simultaneously solving the four nights with high photometric quality and allowing the extinction term for each night to vary separately. The resulting photometric solutions and associated errors (~ 0.02 magnitudes) are given in Table 5. Because of the updated electronics between 1997 and 1998, the solution for the one photometric night in 1998 was

derived independently.

Even in non-photometric conditions (i.e. any cloud cover visible in any part of the sky), standards were monitored to test our ability to judge the level of cloud cover. The derived “photometric” solutions for the parts of non-photometric nights which were judged to be reasonably clear are listed in parentheses in Table 5. In general, the solutions are nearly identical to those derived for the photometric nights, suggesting that the parts of the night which we considered to be clear had transparencies comparable to truly photometric conditions. As a further test, we made plots of the sky level as a function of time during our science exposures. On the photometric nights, the sky level was very stable, varying extremely slowly and smoothly. By comparing our observing logs to plots of the sky level during partially cloudy nights, we found that the presence of clouds produced obvious, rapid variations in the sky level. We used the combination of our observing notes and plots of the sky level to judge the degree of photometric accuracy reported in Table 4.

Unlike the B and R -band results, we were unable to find any infrared observations of our sample galaxies in the literature with which to compare our global calibration. While roughly 1/4 - 1/3 of our sample is visible in the existing 2MASS survey (Skrutskie et al. 1997), these galaxies are so faint and diffuse that they have not been cataloged or photometered.

We have, however, checked our photometric calibration internally. For roughly half of our sample, we obtained images over two or more nights. This was particularly true for the galaxies with the faintest K_s -band surface brightnesses, which required much deeper observations. We have performed aperture photometry on all fields observed on separate nights in order to (1) test the consistency of our photometry and (2) to correct observations taken in non-photometric conditions. The mean amplitude of night-to-night variations among the photometric observations and the “questionable” observations (marked by a “:” in Table 4) were identical ($\Delta|m|=0.04$), and were all within the 2σ uncertainties defined by photon counting and the photometric calibration. There were also no consistent offsets between nights (i.e. the offsets were just as likely to be negative as positive). Only the non-photometric observations marked with double colons in Table 4 showed significant variations, with $\Delta m_{\text{FGC143}}=0.09$, $\Delta m_{\text{FGC256}}=0.31$, $\Delta m_{\text{FGC901}}=0.55$, and $\Delta m_{\text{FGC1971}}=0.28$. The zero points of these non-photometric images were adjusted accordingly before they were coadded with the photometric data. We also did not include the data for FGC 1303 from 980415 and for FGC 277 from 971015, as unfortunately, the sub-images could not be properly aligned.

5. Masking

In order to facilitate analysis of the galaxy profiles at low light levels, we generated a mask for each image, to identify regions contaminated by interloping sources (stars, galaxies, meteor trails, etc.). The masks were made using our R band images, which typically had the highest signal-to-noise. First, SExtractor (Bertin & Arnouts 1996) was used to identify all objects in the frame. Using the reported ellipticities and isophotal areas, we masked elliptical regions around all detected objects (except for the immediate vicinity of the central galaxy where objects were masked by hand to avoid masking HII regions associated with the galaxy). We increased the size of the masked regions by a factor of three, producing a factor of 9 increase in the area, and thus reducing any contamination from interloper objects at low light levels.

The resulting masks were then visually inspected, and edited by hand to remove any remaining sources of contamination in all three bands (i.e. B , R , & K_s). Examples of these include objects which fell on top of or very near to a galaxy (a problem in lower latitude fields), meteor trails, diffraction spikes from bright stars, poorly removed bad columns, obvious scattered light from stars just off the field, and regions which were not covered in all three sub-exposures used to make the final optical images. There is some ambiguity about removing faint “contaminating” objects close to the galaxy, given the natural confusion between faint intervening galaxies and small HII regions within the galaxy. This confusion is highest in the furthest outskirts of the galaxies, which are known to harbor faint HII regions, in spite of having little diffuse optical emission (e.g. Ferguson et al. 1998). We typically mask these regions when there was no diffuse emission connecting the faint object to the main galaxy. Given that these sources are all extremely faint, their inclusion or exclusion will make little difference in the total magnitude of the galaxy. They may slightly affect the shapes of the faintest isophotes, however.

We also generated a second set of masks to generously encompass the faintest possible isophotes of the main FGC galaxy. These masks are used to exclude all possible contributions from the galaxy when measuring the background sky.

Finally, for each galaxy, identical masks were used for all bands, so that all analysis was restricted to the same portions of the images.

6. Sky Subtraction

After the B and R images were flattened using the combination of dome flats, twilight flats, and supersky flats, there remained residual diffuse low surface brightness structure

visible in many of the images. These structures varied significantly from image to image, and are thus not due to variations in the illumination or the response of the CCD. In most cases, the position of the structure shifts with the sky in the series of dithered images, suggesting these sky fluctuations are an astronomical source and not a calibration problem. These remaining variations are most likely the result of a combination of scattered light from stars beyond the field of view, and optical emission from the 100μ cirrus (e.g. Guhathakurta et al. 1990). These unavoidable sources of non-uniform background represent a fundamental limit on our ability to trace the structure of galaxies to extremely low surface brightnesses ($\mu(R) > 28 \text{ mag/arcsec}^2$).

Because these sources are additive, we have made a first-order attempt to subtract them from the B and R images by fitting a plane to the 982×982 pixel subregion around each galaxy. The images were masked with both the background object mask and the galaxy mask (§5), leaving only sky pixels in the resulting image. A plane was then fit to the unmasked background, using iterative rejection of outliers. The resulting slopes implied a variation across the $4.2'$ region of typically fainter than $\Delta\mu > 29 B \text{ mag/arcsec}^2$ and $\Delta\mu > 27 R \text{ mag/arcsec}^2$. These surface brightness variations are also characteristic of the smaller scale structures found in some of the images.

We chose not to perform a further background subtraction on the K_s band images. Because of the smaller field of view of the infrared images and our generous masking of the galaxy region, the number of unmasked “background” pixels was small, leading to unrepresentative fits to the overall background. The unmasked pixels were typically found in the outskirts of the image, which were sampled by a much smaller number of sub-images, and thus were of lower signal-to-noise and more prone to statistical variations in the sky level. Furthermore, given the higher level of ghosting and scattered light in the IRCAM (compared to the optical CCD camera) and the brighter IR sky, remaining sky variations are more likely to be calibration problems than true astronomical signals. Experiments quickly revealed that fitting the sky background with the same procedure used for the optical bands created gradients across the central field, rather than eliminating them.

7. Isophotes and Integrated Magnitudes

Before defining magnitudes for the galaxies in our sample, it was necessary to define isophotal contours for photometry. Using IDL, we defined contour levels in the masked, unsmoothed image, down to an isophote level of 3σ above the sky. To trace the contours to fainter limits, we developed a variable smoothing method, wherein the image was smoothed with a Gaussian ellipse whose size was adjusted to preserve constant signal-to-noise in the

resulting image, with the maximum smoothing length fixed to a width of 15 pixels (3.9'') and a 3:1 axial ratio oriented along the major axis of the galaxy. Note, however, that while smoothing was used to set the shape of the faintest isophotes, photometry was performed only on the unsmoothed images. We also did not correct the levels of the isophotes to compensate for foreground Galactic extinction; the isophotes therefore refer to an apparent surface brightness, rather than one intrinsic to the galaxy.

The resulting isophotes are plotted in Figure 3. The plots clearly show the transition between using smoothed and unsmoothed isophotes, as individual pixels mark the edge of the latter, and smoother contiguous lines mark the former. Occasionally, contours skirt the perimeters of masked stars, leading to odd shapes in the isophotes. To partially compensate for the flux lost to masking, and to better trace the isophotes, we derived approximate smooth models for the galaxies in an attempt to “fill” in the masked regions. As this process is necessarily uncertain, we include the magnitude of the flux added by the model in our uncertainties; rarely is this contribution the dominant source of error.

Using these isophotes, we have derived isophotal magnitudes in B , R , and K_s . We present these in Table 6 for our sample, uncorrected for galactic extinction. We give magnitudes in reference to a specific isophotal level in each band ($\mu_{lim}(B)=27$ mag/arcsec², $\mu_{lim}(R)=26$ mag/arcsec², and $\mu_{lim}(K)=22$ mag/arcsec²), in order to facilitate comparison with other comparable observations, most notably the Ursa Major cluster sample of Verheijen (1997). Because the isophotal areas associated with these limits are a strong function of the filter bandpass, we also give magnitudes in B and K_s which are calculated within the area of the $\mu_{lim}(R)=25$ mag/arcsec² isophote; these magnitudes should be used when determining colors for the sample. In a few cases, due to somewhat shallower observations or larger problems with scattered light (e.g. FGC 2292), the reference isophotes were not reliably determined; these cases are left blank in Table 6. Because projection makes the galaxies in this edge-on sample appear brighter, the isophotes of our sample probably occur at larger radii than they would if seen face-on, and are thus comparable to fainter isophotes for less inclined galaxies. We have chosen not to correct the final magnitudes listed in Table 6 to either total or face-on values, as such conversions would be highly uncertain.

In calculating the magnitudes, we have included the color term in the zero point by first calculating the magnitudes assuming a mean color of $B - R \sim 1$ and $J - K_s \sim 1$, and then making a second order correction (typically less than 0.02) based upon the resulting color of the galaxy within the $\mu_{lim}(R)=25$ mag/arcsec² isophote. As we did not have information on the $J - K_s$ colors of the sample, we made no further correction to the infrared K_s magnitudes.

Because the amplitude of Galactic extinction corrections tend to be a function of time and a matter of taste, we have listed $E(B - V)$ from Schlegel et al. (1998) in Table 6, but have not include the associated correction in the B , R , or K_s values in Table 6.

7.1. Uncertainties & Reliability of Faint Isophotes

There are three main sources which contributed to the uncertainties given in Table 6. First are the photometric calibration uncertainties, σ_m , given in Tables 3 & 5, which are typically $\lesssim 0.02$ in the optical and $\lesssim 0.05$ in the infrared. The value of σ_m is the RMS scatter around the photometric solution, and is an empirical measurement of the characteristic error in an individual measurement. Thus, σ_m is a conservative estimate of the photometric uncertainty associated with any single observation.

The second source of uncertainty comes from the area lost to masking of stars on or near the galaxy, or to the small area of the K_s image (smaller than the extent of the R -band isophotes in some cases). Both effects cause flux to be underestimated. In most instances, the galaxies in our sample are at high enough galactic latitude that few foreground stars overlap even the faintest isophotes of the galaxy, and thus this is usually not a problem. However, we have attempted to correct for this effect, by using the smoothed models described above to interpolate within the masked regions. While this process is uncertain, it is at least a step in the right direction. Furthermore, the magnitude of the correction gives some indication of the magnitude of the uncertainty. Typically, these corrections are less than 0.05 magnitudes.

The final, most subtle, and dominant source of uncertainty comes from sky subtraction. If the level of the sky is wrong, then this contributes/removes additional light to/from the galaxy, in proportion to the area of the isophote used for photometry. To set the uncertainty in the sky subtraction, we have analyzed the noise properties of the unmasked “sky” pixels (see §6) for a variety of boxcar smoothing lengths, L (Figure 4). For an uncorrelated, uniform sky background, the standard deviation of the sky pixels, σ_{sky} , will decrease with increasing smoothing lengths as $1/L$; this relation is plotted as the dashed line in Figure 4. For a highly correlated, non-uniform sky background, σ_{sky} will be constant as long as L is smaller than scale of the non-uniformity, and the Poisson fluctuations in the smoothed image are smaller than the amplitude of the non-uniformity (for example, imagine a step-function in brightness across the image). Mathematically, for a given power spectrum of background sky fluctuations, the predicted distribution of $\sigma_{\text{sky}}(L)$ can be calculated in analogy to the “counts-in-cells” formalism developed for large-scale structure analysis (e.g. Peebles 1980). The inclusion of the correlated background increases the variance above

that predicted for pure Poisson fluctuations by adding a term involving the integral of the correlation function over the smoothing area. In each image, we can therefore assess the level of residual structure in the sky and its origin from the behavior of $\sigma_{\text{sky}}(L)$, shown in Figure 4. These plots also indicate the reliability of surface photometry at various length scales.

The plots of $\sigma_{\text{sky}}(L)$ in Figure 4 reveal a number of facts about our data. First, there is indeed correlated structure in the sky, as revealed by the deviation of the measured curves from the $1/L$ behavior expected for a uniform Poisson background. The presence of such structures is not too surprising, given that we fully expect to have residual contamination from scattered light and from stars and galaxies which lie below our detection threshold.

Second, the similarity of the B and R band $\sigma_{\text{sky}}(L)$ curves, down to the faintest surface brightnesses, suggests that the deviation from the $1/L$ Poisson expectation does not result from uncertainties in flat-fielding, at least for the optical imaging. Large-scale flat-fielding errors would be expected to differ between the two bands, leading to shape variations for observations taken through different filters. These shape variations would be consistent, however, for all galaxies observed on a single night. Although we do see occasional variations in between the shape of the B and R curves (c.f. FGC 51), these variations are not consistent with other galaxies observed on the same night. Thus, they are more realistically interpreted as being variations in the scattered light in the different bands (see below), given that the pointing centers are not identical for the sub-images used to make the B and R images.

Third, we also see many cases where the curve is rolling over to flat as we approach the amplitude of the background sky variations. In some cases (e.g. FGC 227, FGC 2548, FGC E1371, FGC E1404, & FGC E1440), optical emission from 100μ cirrus is clearly visible in the frame. In others (c.f. FGC 51, FGC 2264, & FGC 1642), scattered light is a large problem in one of the sub-images. In all of these cases, $\sigma_{\text{sky}}(L)$ rolls over at large smoothing lengths, as expected, and reveals the characteristic brightness of the structure.

Finally, the plots in Figure 4 clearly demonstrate the well known difficulties with attempting to do reliable infrared surface photometry of nearby galaxies. The small field-of-view of IR detectors, the brightness and variability of the IR sky, and the difficulty in constructing reasonable dome flats all conspire to make the prospect of accurate faint surface brightnesses photometry daunting, if not practically impossible with current detectors. The K_s -band $\sigma_{\text{sky}}(L)$ curves deviate in shape from the optical curves at relatively small smoothing lengths ($\sim 5''$) and bright surface brightnesses ($\mu_{K_s} \lesssim 22 \text{ mag/arcsec}^2$), demonstrating the limitations of our K_s -band data at large scales and faint surface brightnesses. Because of mosaicking, the signal-to-noise of the K_s images tends to degrade towards the outskirts of the image, away from the galaxy. The estimates of the sky

uncertainty come from these outer regions, and will thus be biased towards higher values. Thus, sky subtraction near the galaxy is therefore likely to be somewhat better than indicated by Figure 4.

To treat the contribution that the uncertainties in sky subtraction make to the magnitudes in Table 6, we take the faintest, reliably-determined value of $\sigma_{sky}(L)$ (i.e. the highest point in each curve plotted in Figure 4) as being characteristic of the error in our determination of the sky. We then calculate the uncertainty in the total flux over the isophotal area.

8. Summary

In this first of a series of papers, we have described our sample of edge-on, late-type disk galaxies. As we have demonstrated, the optical and infrared imaging data on these galaxies is exceptionally well characterized, and will be well suited for upcoming analysis of the structural properties of the sample, down to very faint surface brightness limits ($\mu(B) \sim 29.5 \text{ mag/arcsec}^2$, $\mu(R) \sim 29 \text{ mag/arcsec}^2$).

Acknowledgements

First and foremost, we are deeply indebted to the generous allocations of telescope time made by Carnegie Observatories during the course of this project. Likewise, the success of this work was dependent upon the excellent instrumentation and telescopes maintained by the staff at Carnegie and at Las Campanas, and its execution would not have been nearly as smooth without the expert help of Herman Olivares and Fernando Peralta. We are also grateful to the hospitality of Casa Polacka during times of inclement weather, and to Scott Trager for his company during the near fatal empanada excursion during the October 1997 observing run. Eric Deutsch is warmly thanked for help with IDL, as is Dan Rosenthal for spirited discussions.

JJD was partially supported through NSF grant AST-990862, and submitted this paper while at the Institute for Theoretical Physics at UC Santa Barbara, which is supported in part by the National Science Foundation under Grant No. PHY94-07194. Support for RAB was provided by NASA through Hubble Fellowship grant HF-01088.01-97A awarded by STScI, which is operated by AURA, Inc. for NASA under contract NAS 5-2655. This research has made use of the NASA/IPAC Extragalactic Database (NED) which is operated by the Jet Propulsion Laboratory, California Institute of Technology, under contract with the National Aeronautics and Space Administration. This paper also made use of the

Digitized Sky Surveys, which were produced at the Space Telescope Science Institute under U.S. Government grant NAG W-2166. The images of these surveys are based on photographic data obtained using the Oschin Schmidt Telescope on Palomar Mountain and the UK Schmidt Telescope. The plates were processed into the present compressed digital form with the permission of these institutions. The National Geographic Society - Palomar Observatory Sky Atlas (POSS-I) was made by the California Institute of Technology with grants from the National Geographic Society.

9. References

- Bahcall, J. N. 1984, *ApJ*, 276, 156.
- Bertin, E., & Arnouts, S. 1996, *Astr. Ap. Suppl.*, , 117, 393.
- de Blok, E., & van der Hulst, J. M. 1998, *Astr. Ap.*, , 336, 49.
- de Blok, E., & McGaugh, S. S. 1997, *MNRAS*, 290, 533.
- de Grijs, R., 1998, *MNRAS*, 299, 595.
- Dove, J. B., & Thronson, H. A. 1993, *ApJ*, 411, 632.
- Ferguson, A. M. N., Wyse, R. F. G., Gallagher, J. S., & Hunter, D. A. 1998, *ApJ*, 506, 19.
- Freeman, K. C. 1970, *ApJ*, 160, 811.
- Goad, J. W., & Roberts, M. S. 1981, *ApJ*, 250, 79.
- Giovanelli, R., Avera, E. & Karachentsev, I. D. 1997, *AJ*, 114, 122.
- Guhathakurta, P., Tyson, J. A., & Majewski, S. R. 1990, *ApJ*, 357, 9.
- Haynes, M. P., Giovanelli, R., Herter, T., Vogt, N. P., Freudling, W., Maia, M. A. G., Salzer, J. J., & Wegner, G. 1997, *AJ*, 113, 1197
- Landolt, A. U. 1983, *AJ*, 88, 439.
- Landolt, A. U. 1992, *AJ*, 104, 340.
- Lauberts, A., & Valentijn, E. A. 1989, *The Surface Photometry Catalogue of the ESO-Uppsala Galaxies (ESO-LV)*, ESO.
- Karachentsev, I. D., Karachentseva, V. E., & Parnovsky, S. L. 1993, *Astro. Nacht.*, 314, 97.
- Kudrya, Y. N., Karachentsev, I. D., Karachentseva, V. E., Parnovskii, S. L. 1994, *Astr. Letters.*, 20, 8.
- McGaugh, S. S. 1994, *ApJ*, 426, 135.
- Moshir et al 1990, *IRAS Faint Source Catalog*.
- Murphy, D. C., Persson, S. E., Pahre, M. A., Sivaramakrishnan, A., & Djorgovski, S. G. 1995, *PASP*, 107, 1234.
- Olling, R. P. 1995, *AJ*, 110, 591.
- Persson, S. E., Murphy, D. C., Krzeminski, W., Roth, M., & Rieke, M. J. 1998, *AJ*, 116,

2475.

- Persson, S. E., West, S. C., Carr, D. M., Sivaramakrishnan, A., & Murphy, D. C. 1992, PASP, 104, 204.
- Schlegel, D. J., Finkbeiner, D. P., & Davis, M. 1998, ApJ, 500, 525.
- Schneider, S. E., Thuan, T. X., Magri, C., & Wadiak, J. E. 1990, ApJS, 72, 245.
- Skrutskie, M.F., Schneider, S.E., Stiening, R., Strom, S.E., Weinberg, M.D., Beichman, C., Chester, T., Cutri, R., Lonsdale, C., Elias, J., Elston, R., Capps, R., Carpenter, J., Huchra, J., Liebert, J., Monet, D., Price, S. and Seitzer, P. 1997, in "The Impact of Large Scale Near-IR Sky Surveys," p187-195, F. Garzon *et al.* eds. (Dordrecht: Kluwer).
- Spitzer, L., 1942 ApJ, 95, 329.
- Swaters, R. A., Madore, B. F., & Trewhella, M. 2000, ApJ, 531, 107L.
- van den Bosch, F. C., Robertson, B. E., Dalcanton, J. J., & de Blok, W. J. G. 2000, AJ, 119, 1579.
- van der Kruit, P. C., & Searle L. 1982, Astr. Ap., , 110, 61.
- van der Kruit, P. C., & de Grijs, R. 1999, Astr. Ap., , 352, 129.
- Verheijen, M. A. W. 1997, PhD Thesis, University of Groningen.
- Zasov, A. V., Makarov, D. I., & Mikhailova, E. A. 1991, Sov. Astron. Lett., 17, 5.
- Zwaan, M. A., van der Hulst, J. M., de Blok, W. J. G., & McGaugh, S. S 1995, MNRAS, 273, L35.

Table 1. Survey Galaxies

| FGC | UGC | α (1950.0) | δ (1950.0) | PA (deg) | V_{\odot} km/s | $W_{50,c}$ km/s |
|-------|-------|----------------------|----------------------|-------------|---------------------|--------------------|
| 31 | | 00:17:00.2 | +18:22:53 | 34 | 5287 | 143 |
| 36 | | 00:19:34.0 | +10:06:15 | 149 | 5446 | 191 |
| 51 | 290 | 00:26:32.3 | +15:37:32 | 133 | 767 | 69 |
| 84 | | 00:42:07.2 | -11:27:43 | 48 | - | - |
| 130 | | 01:08:17.0 | +14:01:04 | 22 | - | - |
| 143 | 819 | 01:13:24.0 | +06:22:50 | 74 | 2417 | 97 |
| 164 | 971 | 01:22:14.7 | +00:46:27 | 148 | 4735 | 119 |
| 215 | 1417 | 01:53:58.4 | +17:28:01 | 153 | 11430 | 300 |
| 225 | 1484 | 01:57:41.0 | +15:43:23 | 106 | 5063 | 172 |
| 227 | | 01:58:12.5 | +19:27:50 | 9 | 5620 | 214 |
| 256 | 1677 | 02:08:26.0 | +06:25:56 | 135 | 1608 | 77 |
| 277 | | 02:17:02.4 | +18:45:05 | 136 | - | - |
| 310 | | 02:29:56.5 | +15:29:58 | 78 | 5873 | 202 |
| 349 | | 02:48:43.3 | +05:21:02 | 173 | 8114 | 212 |
| 395 | 2548 | 03:09:10.1 | +00:51:29 | 134 | - | - |
| 436 | | 03:32:00.9 | +14:58:25 | 169 | 6218 | 243 |
| 442 | | 03:37:57.7 | +03:22:33 | 136 | 5733 | 205 |
| 446 | 2852 | 03:42:16.0 | +05:44:54 | 119 | 6101 | 334 |
| 780 | 4524 | 08:37:35.5 | +05:48:43 | 50 | 1939 | 150 |
| 901 | | 09:29:17.5 | +12:28:57 | 170 | 5899 | 201 |
| 913 | | 09:33:46.6 | +15:46:21 | 175 | 4329 | 154 |
| 979 | 5347 | 09:54:40.5 | +04:45:53 | 18 | 2156 | 210 |
| 1043 | 5537 | 10:13:04.2 | +07:34:33 | 146 | 3755 | 288 |
| 1063 | | 10:21:55.7 | +12:09:56 | 168 | 2431 | 140 |
| 1285 | 6594 | 11:35:03.3 | +16:50:00 | 134 | 1040 | 150 |
| 1303 | | 11:43:32.9 | +13:09:24 | 115 | 3290 | 134 |
| 1415 | 7394 | 12:17:54.0 | +01:44:40 | 146 | 1598 | 173 |
| 1440 | 7607 | 12:26:19.4 | +04:34:02 | 53 | 4240 | 301 |
| 1642 | | 13:33:32.4 | +08:26:33 | 139 | 1243 | 110 |
| 1863 | 9760 | 15:09:30.3 | +01:53:11 | 55 | 2023 | 137 |
| 1945 | 10000 | 15:42:18.8 | +04:06:54 | 124 | 3541 | 206 |
| 1948 | 10025 | 15:43:53.0 | +03:00:00 | 81 | 1522 | 109 |
| 1971 | 10111 | 15:55:53.4 | +13:18:41 | 37 | 10387 | 454 |
| 2131 | 10852 | 17:23:56.6 | +11:21:35 | 163 | 2781 | 139 |
| 2135 | | 17:25:06.6 | +13:42:17 | 124 | 9059 | 222 |
| 2217 | 11301 | 18:35:42.2 | +17:29:22 | 110 | 4500 | 478 |
| 2264 | | 19:47:00.6 | -10:54:02 | 127 | - | - |
| 2292 | | 20:52:36.3 | +17:28:02 | 170 | 5563 | 174 |
| 2367 | | 22:05:34.8 | +15:28:14 | 25 | 7827 | 159 |
| 2369 | | 22:07:21.6 | +07:11:01 | 83 | - | - |
| 2548 | | 23:49:47.6 | +07:41:54 | 113 | 3865 | 142 |
| 2558 | | 23:52:46.0 | +03:32:38 | 58 | 5378 | 178 |
| E1371 | | 19:18:33.6 | -38:18:07 | 141 | - | - |
| E1404 | | 19:46:40.1 | -36:30:16 | 35 | - | - |
| E1440 | | 20:08:56.0 | -22:46:12 | 10 | - | - |
| E1447 | | 20:12:16.6 | -55:13:25 | 23 | - | - |
| E1498 | | 20:35:21.0 | -53:26:31 | 64 | - | - |
| E1619 | | 21:32:44.7 | -28:55:56 | 149 | - | - |
| E1623 | | 21:33:58.0 | -19:49:30 | 12 | - | - |

Table 2. Optical Observations

| FGC | Exp (<i>B</i>) <i>s</i> | Exp (<i>R</i>) <i>s</i> | μ_{sky} (<i>B</i>) mag/arcsec ² | σ_{μ} (<i>B</i>) rms per \square'' | μ_{sky} (<i>R</i>) mag/arcsec ² | σ_{μ} (<i>R</i>) rms per \square'' | FWHM (<i>B</i>) " | FWHM (<i>R</i>) " |
|-------|------------------------------|------------------------------|---|--|---|--|------------------------|------------------------|
| 31 | 900 | 360 | 22.6 | 27.6 | 20.7 | 26.5 | 1.0 | 0.9 |
| 36 | 900 | 600 | 22.6 | 27.5 | 20.6 | 26.8 | 1.1 | 0.8 |
| 51 | 900 | 960 | 22.3 | 27.0 | 20.4 | 26.7 | 1.1 | 0.8 |
| 84 | 900 | 480 | 21.9 | 27.3 | 20.8 | 26.6 | 0.9 | 0.7 |
| 130 | 900 | 360 | 22.5 | 27.3 | 20.4 | 26.2 | 1.0 | 1.0 |
| 143 | 900 | 240 | 22.5 | 27.4 | 20.4 | 26.3 | 1.0 | 0.9 |
| 164 | 900 | 360 | 21.4 | 27.0 | 20.4 | 26.3 | 1.1 | 1.0 |
| 215 | 900 | 360 | 21.0 | 26.8 | 20.2 | 26.1 | 1.4 | 1.1 |
| 225 | 900 | 360 | 21.5 | 27.0 | 20.2 | 26.3 | 1.1 | 0.9 |
| 227 | 900 | 360 | 22.4 | 27.3 | 20.1 | 26.2 | 1.3 | 1.1 |
| 256 | 900 | 600 | 21.5 | 27.1 | 20.3 | 26.4 | 1.1 | 1.0 |
| 277 | 900 | 600 | 22.4 | 27.4 | 20.1 | 26.3 | 1.1 | 1.0 |
| 310 | 900 | 360 | 22.1 | 26.9 | 20.1 | 26.1 | 1.2 | 0.9 |
| 349 | 900 | 360 | 21.4 | 27.0 | 20.3 | 26.3 | 1.1 | 0.8 |
| 395 | 900 | 360 | 21.9 | 26.9 | 20.3 | 26.3 | 1.0 | 0.8 |
| 436 | 300 | 240 | 20.6 | 25.9 | 19.7 | 25.8 | 1.3 | 1.0 |
| 442 | 900 | 240 | 21.2 | 26.8 | 20.2 | 25.9 | 1.3 | 0.8 |
| 446 | 900 | 360 | 21.1 | 26.7 | 20.2 | 26.2 | 1.5 | 0.9 |
| 780 | 2100 | 900 | 22.3 | 27.7 | 20.4 | 26.8 | 0.7 | 0.7 |
| 901 | 1800 | 600 | 22.1 | 27.8 | 20.5 | 26.7 | 1.2 | 0.9 |
| 913 | 1800 | 900 | 22.2 | 27.7 | 20.3 | 26.9 | 0.8 | 0.7 |
| 979 | 1800 | 600 | 22.4 | 27.7 | 20.6 | 26.6 | 0.8 | 0.7 |
| 1043 | 900 | 360 | 22.3 | 27.3 | 20.6 | 26.4 | 0.9 | 0.9 |
| 1063 | 900 | 720 | 22.3 | 27.3 | 20.5 | 26.9 | 1.0 | 0.7 |
| 1285 | 1800 | 900 | 22.3 | 27.7 | 20.6 | 27.0 | 1.0 | 1.1 |
| 1303 | 2700 | 900 | 22.2 | 28.0 | 20.7 | 26.9 | 0.9 | 0.8 |
| 1415 | 900 | 360 | 22.2 | 27.2 | 20.7 | 26.6 | 0.9 | 0.8 |
| 1440 | 1800 | 900 | 22.3 | 27.8 | 20.7 | 27.0 | 0.8 | 0.7 |
| 1642 | 2700 | 600 | 22.3 | 27.8 | 20.7 | 26.7 | 1.0 | 0.7 |
| 1863 | 2700 | 900 | 22.4 | 28.1 | 20.8 | 27.0 | 0.8 | 0.7 |
| 1945 | 1800 | 600 | 22.4 | 27.9 | 20.8 | 26.8 | 0.8 | 0.8 |
| 1948 | 2700 | 900 | 22.4 | 28.0 | 20.7 | 26.8 | 1.0 | 0.8 |
| 1971 | 2700 | 900 | 22.4 | 28.1 | 20.7 | 26.9 | 0.9 | 0.9 |
| 2131 | 2700 | 900 | 22.3 | 27.8 | 20.6 | 26.7 | 1.3 | 1.0 |
| 2135 | 1800 | 600 | 22.3 | 27.9 | 20.7 | 26.7 | 0.9 | 0.8 |
| 2217 | 900 | 360 | 22.1 | 26.5 | 20.5 | 25.7 | 1.3 | 1.3 |
| 2264 | 900 | 360 | 22.4 | 26.2 | 20.8 | 25.7 | 0.8 | 0.7 |
| 2292 | 900 | 360 | 22.6 | 27.3 | 20.7 | 26.2 | 0.9 | 0.8 |
| 2367 | 900 | 360 | 22.7 | 27.3 | 20.7 | 26.3 | 1.0 | 0.9 |
| 2369 | 900 | 360 | 22.7 | 27.5 | 20.9 | 26.4 | 1.1 | 0.8 |
| 2548 | 900 | 360 | 22.5 | 27.5 | 20.9 | 26.7 | 0.9 | 0.8 |
| 2558 | 900 | 360 | 22.5 | 27.4 | 20.8 | 26.4 | 1.0 | 0.8 |
| E1371 | 900 | 360 | 22.4 | 27.5 | 20.7 | 26.3 | 0.9 | 0.9 |
| E1404 | 900 | 360 | 22.4 | 27.4 | 20.7 | 26.2 | 1.2 | 0.9 |
| E1440 | 900 | 360 | 22.4 | 27.3 | 20.6 | 26.3 | 0.9 | 0.8 |
| E1447 | 900 | 360 | 22.7 | 27.6 | 21.0 | 26.6 | 0.8 | 0.8 |
| E1498 | 900 | 360 | 22.8 | 27.6 | 21.0 | 26.4 | 0.9 | 0.8 |
| E1619 | 900 | 240 | 22.6 | 27.5 | 21.0 | 26.2 | 1.0 | 0.8 |
| E1623 | 900 | 360 | 22.5 | 27.3 | 20.9 | 26.5 | 1.0 | 0.8 |

Table 3. Optical Photometric Solutions:
 $m = -2.5 * \log(DN/sec) + m_{zp} + X * Airmass + Y * (B - R)$

| UT Date | Filter | N_{stars} | m_{zp} | X | Y | σ_m |
|---------|----------|-------------|----------|--------|--------|------------|
| 970923 | <i>B</i> | 45 | 24.158 | -0.194 | 0.046 | 0.015 |
| 970924 | <i>B</i> | 29 | 24.158 | -0.204 | 0.046 | 0.016 |
| 980330 | <i>B</i> | 38 | 24.114 | -0.237 | 0.044 | 0.016 |
| 980331 | <i>B</i> | 36 | 24.093 | -0.231 | 0.044 | 0.020 |
| 970923 | <i>R</i> | 38 | 24.501 | -0.069 | -0.003 | 0.012 |
| 970924 | <i>R</i> | 38 | 24.501 | -0.086 | -0.003 | 0.015 |
| 980330 | <i>R</i> | 46 | 24.439 | -0.095 | -0.002 | 0.020 |
| 980331 | <i>R</i> | 57 | 24.438 | -0.093 | -0.002 | 0.020 |

Table 4. Infrared Observations

| FGC | Exp Time (min) | Date (UT) | FWHM _{major} (K_s) ($''$) | a/b_{PSF} | PA _{PSF} (degrees) |
|------|-------------------|--------------|---|--------------------|--------------------------------|
| 31 | 48 | 970921 | 1.1 | 1.5±0.6 | -85±35 |
| 36 | 16: | 971011 | 0.7 | 1.1±0.1 | -53±39 |
| 51 | 22: | 971011 | 1.3 | 1.7±0.1 | 46±37 |
| 84 | 36 | 970922 | 0.7 | 1.1±0.1 | -52±14 |
| 130 | 12: | 971011 | | | |
| | 8 | 971012 | (1.1) | (1.1±0.1) | (77±77) |
| 143 | 20:: | 971011 | | | |
| | 24 | 971012 | 1.0 | 1.1±0.1 | -73±100 |
| 164 | 24 | 971012 | 1.1 | 1.1±0.1 | 47±17 |
| 215 | 18 | 970922 | - | - | - |
| 225 | 30 | 971012 | (1.2) | (1.2±0.2) | (18±18) |
| | 20 | 971015 | | | |
| 227 | 24 | 970921 | - | - | - |
| | 12 | 971015 | | | |
| 256 | 24:: | 971011 | | | |
| | 38 | 971012 | 1.1 | 1.1±0.1 | 81±80 |
| | 36 | 971015 | | | |
| 277 | 30 | 970921 | 1.1 | 1.1±0.1 | -84±86 |
| | 30 | 971015 | | | |
| 310 | 24 | 970921 | 0.8 | 1.7±0.7 | 71±23 |
| 349 | 38: | 971011 | 0.9 | 1.1±0.1 | -70±20 |
| | 12 | 971012 | | | |
| 395 | 24 | 970921 | 0.8 | 1.5±0.4 | 34±10 |
| | 18 | 971015 | | | |
| 436 | 24 | 970922 | 1.0 | 1.1±0.1 | -63±46 |
| 442 | 12: | 971011 | | | |
| | 24 | 971012 | 1.0 | 1.5±0.7 | 85±69 |
| 446 | 12 | 970922 | (0.8) | (1.2±0.2) | (-59±59) |
| 780 | 24 | 980415 | 1.2 | 1.2±0.2 | -33±15 |
| 901 | 18:: | 980414 | | | |
| | 18 | 980415 | - | - | - |
| 913 | 18 | 980415 | 0.9 | 2.0±0.6 | 86±58 |
| 979 | 12 | 980415 | 1.0 | 1.0±0.1 | -26±23 |
| 1043 | 12 | 980415 | 1.0 | 1.8±0.6 | -11±5 |
| 1063 | 18 | 980415 | 1.1 | 1.5±0.5 | 89±5 |
| 1285 | 18 | 980415 | 1.0 | 1.0±0.1 | -52±5 |
| 1303 | 12: | 980414 | | | |
| | 18 | 980415 | 0.9 | 1.2±0.3 | 78±19 |
| 1415 | 10 | 980415 | 1.0 | 1.2±0.1 | -72±58 |
| 1440 | 10 | 980415 | 1.1 | 2.0±0.7 | -58±37 |
| 1642 | 12: | 980414 | | | |
| | 20 | 980415 | 0.8 | 1.9±0.4 | 66±53 |
| 1863 | 18 | 980415 | 1.2 | 1.5±0.5 | -52±55 |
| 1945 | 12: | 980414 | | | |
| | 18 | 980415 | 0.9 | 1.5±0.6 | 83±61 |
| 1948 | 12: | 980414 | | | |
| | 18 | 980415 | 1.1 | 1.9±0.7 | 82±72 |
| 1971 | 8:: | 980414 | | | |
| | 30 | 980415 | 1.1 | 1.6±0.6 | 59±47 |
| 2131 | 18 | 980415 | 1.2 | 1.4±0.1 | 69±4 |

Table 4—Continued

| FGC | Exp Time (min) | Date (UT) | FWHM _{major} (K_s) ($''$) | a/b_{PSF} | PA _{PSF} (degrees) |
|-------|-------------------|--------------|---|--------------------|--------------------------------|
| 2135 | 18 | 980415 | 1.0 | 1.3 \pm 0.2 | 59 \pm 56 |
| 2217 | 12 | 980415 | 1.0 | 1.4 \pm 0.2 | 12 \pm 4 |
| 2264 | 12 | 970921 | 1.0 | 1.3 \pm 0.2 | 46 \pm 34 |
| 2292 | 24 | 970921 | 0.9 | 1.3 \pm 0.2 | 91 \pm 26 |
| 2367 | 18 | 971011 | 1.1 | 1.1 \pm 0.2 | 87 \pm 49 |
| | 38 | 971012 | | | |
| 2369 | 36 | 970921 | 1.0 | 1.2 \pm 0.2 | 59 \pm 75 |
| 2548 | 36 | 970921 | | | |
| | 48 | 971012 | 1.2 | 1.2 \pm 0.1 | 28 \pm 7 |
| 2558 | 18: | 971011 | | | |
| | 36 | 971012 | 0.5 | 1.1 \pm 0.2 | -26 \pm 20 |
| E1371 | 18 | 970922 | 1.2 | 1.4 \pm 0.1 | 60 \pm 3 |
| E1404 | 18 | 971011 | | | |
| | 30 | 971012 | 0.9 | 1.1 \pm 0.1 | 59 \pm 14 |
| E1440 | 30 | 970922 | 1.1 | 1.2 \pm 0.2 | -67 \pm 20 |
| | 16 | 971015 | | | |
| E1447 | 30 | 970921 | 0.9 | 1.2 \pm 0.1 | -44 \pm 12 |
| E1498 | 18 | 970922 | 0.8 | 1.1 \pm 0.1 | 74.4 \pm 4.2 |
| E1619 | 18 | 971011 | 1.1 | 1.2 \pm 0.2 | -66 \pm 46 |
| E1623 | 18 | 971011 | 0.9 | 1.1 \pm 0.1 | -25 \pm 25 |

Note. — Single colons (“:”) indicate data taken during clear portions of non-photometric nights. Double colons (“::”) indicate taken during non-photometric conditions. See discussion in §4.3

Table 5. Infrared Photometric Solutions:
 $m = -2.5 * \log(DN/sec) + m_{zp} + X * Airmass + Y * (J - K_s)$

| UT Date | Filter | N_{stars} | m_{zp} | X | Y | σ_m |
|---------|--------|-------------|----------|----------|----------|------------|
| 970922 | K_s | 46 | 21.790 | -0.077 | -0.067 | 0.023 |
| 970923 | K_s | 25 | 21.790 | -0.072 | -0.067 | 0.023 |
| 971011 | K_s | 48 | (21.793) | (-0.065) | (-0.060) | (0.016) |
| 971012 | K_s | 28 | 21.790 | -0.071 | -0.067 | 0.023 |
| 971015 | K_s | 28 | 21.790 | -0.076 | -0.067 | 0.023 |
| 980414 | K_s | 19 | (21.006) | (-0.086) | (-0.067) | (0.027) |
| 980415 | K_s | 46 | 20.950 | -0.058 | -0.067 | 0.045 |

Table 6. Galaxy Magnitudes

| FGC | $m_{R25}(B)$ | $m_{R25}(R)$ | $m_{R25}(K)$ | $m_{B27}(B)$ | $m_{R26}(R)$ | $m_{K22}(K)$ | $E(B - V)$ |
|-------|--------------|--------------|--------------|--------------|--------------|--------------|------------|
| 31 | 17.58±0.02 | 16.90±0.03 | 15.15±0.46 | 17.52±0.03 | 16.83±0.03 | 15.42±0.27 | 0.053 |
| 36 | 17.45±0.02 | 16.32±0.01 | 13.84±0.18 | 17.43±0.02 | 16.30±0.01 | 13.76±0.21 | 0.123 |
| 51 | 16.64±0.02 | 15.84±0.02 | 13.79±0.51 | 16.54±0.03 | 15.72±0.03 | 13.90±0.32 | 0.107 |
| 84 | 17.57±0.02 | 16.69±0.02 | 14.60±0.17 | 17.52±0.03 | 16.64±0.02 | 14.76±0.11 | 0.029 |
| 130 | 17.73±0.04 | 16.20±0.03 | 12.92±0.05 | 17.72±0.04 | 16.18±0.03 | 12.86±0.07 | 0.049 |
| 143 | 17.50±0.07 | 16.45±0.08 | 14.42±0.24 | 17.43±0.07 | 16.37±0.07 | 14.70±0.17 | 0.049 |
| 164 | 17.89±0.02 | 17.19±0.02 | 15.24±0.28 | 17.80±0.03 | 17.09±0.03 | 15.56±0.17 | 0.029 |
| 215 | 17.23±0.02 | 16.11±0.02 | 13.40±0.15 | 17.20±0.02 | 16.09±0.02 | 13.33±0.16 | 0.051 |
| 225 | 17.08±0.02 | 16.21±0.02 | 14.11±0.19 | 17.05±0.02 | 16.17±0.03 | 14.18±0.14 | 0.049 |
| 227 | 17.22±0.03 | 15.93±0.02 | 13.37±0.08 | 17.19±0.04 | 15.88±0.03 | 13.39±0.07 | 0.112 |
| 256 | 18.08±0.02 | 17.24±0.01 | 15.24±0.21 | 18.01±0.02 | 17.18±0.02 | 15.47±0.16 | 0.050 |
| 277 | 18.01±0.03 | 16.60±0.02 | 14.10±0.14 | 17.94±0.03 | 16.52±0.03 | 14.10±0.12 | 0.201 |
| 310 | 17.68±0.04 | 16.20±0.04 | 13.40±0.10 | 17.65±0.05 | 16.17±0.04 | 13.35±0.11 | 0.192 |
| 349 | 17.46±0.02 | 16.37±0.02 | 13.99±0.07 | 17.44±0.02 | 16.35±0.02 | 14.00±0.07 | 0.152 |
| 395 | 17.74±0.03 | 16.32±0.03 | 13.48±0.17 | 17.71±0.04 | 16.28±0.03 | 13.50±0.11 | 0.126 |
| 436 | 17.39±0.04 | 16.05±0.03 | 13.30±0.09 | — | 15.99±0.04 | 13.31±0.08 | 0.330 |
| 442 | 17.26±0.02 | 16.12±0.02 | 13.74±0.10 | 17.22±0.02 | 16.10±0.02 | 13.73±0.09 | 0.144 |
| 446 | 16.17±0.02 | 14.68±0.02 | 11.39±0.13 | 16.15±0.02 | 14.67±0.02 | 11.36±0.14 | 0.234 |
| 780 | 15.77±0.07 | 14.88±0.07 | 12.85±0.55 | 15.70±0.09 | 14.83±0.07 | 12.85±0.39 | 0.035 |
| 901 | 17.48±0.03 | 16.37±0.03 | 13.92±0.23 | 17.44±0.04 | 16.34±0.03 | 13.92±0.22 | 0.022 |
| 913 | 17.04±0.02 | 16.10±0.02 | 13.95±0.26 | 17.02±0.02 | 16.08±0.02 | 13.91±0.22 | 0.038 |
| 979 | 15.42±0.02 | 14.36±0.02 | 11.87±0.12 | 15.39±0.02 | 14.35±0.02 | 11.81±0.14 | 0.057 |
| 1043 | 15.37±0.02 | 14.22±0.02 | 11.41±0.15 | 15.33±0.03 | 14.20±0.03 | 11.41±0.12 | 0.010 |
| 1063 | 17.07±0.02 | 16.29±0.02 | 14.15±0.26 | 17.03±0.03 | 16.25±0.03 | 14.20±0.21 | 0.032 |
| 1285 | 14.75±0.02 | 13.75±0.02 | 11.87±2.19 | 14.73±0.02 | 13.72±0.03 | — | 0.013 |
| 1303 | 17.38±0.02 | 16.51±0.02 | 14.35±0.62 | 17.30±0.03 | 16.45±0.02 | 13.75±0.69 | 0.013 |
| 1415 | 15.19±0.02 | 14.21±0.02 | 12.05±0.54 | 15.16±0.02 | 14.18±0.03 | 12.04±0.37 | 0.023 |
| 1440 | 15.75±0.02 | 14.48±0.02 | 11.52±0.15 | 15.72±0.03 | 14.46±0.02 | — | 0.020 |
| 1642 | 16.79±0.04 | 15.79±0.06 | 13.91±0.57 | 16.75±0.05 | — | 13.97±0.37 | 0.033 |
| 1863 | 15.28±0.14 | 14.44±0.16 | 12.53±0.93 | 15.24±0.15 | 14.40±0.16 | — | 0.051 |
| 1945 | 16.66±0.03 | 15.68±0.03 | 13.34±0.46 | 16.59±0.03 | 15.63±0.03 | 13.07±0.44 | 0.075 |
| 1948 | 16.99±0.02 | 16.12±0.02 | 14.10±0.77 | 16.88±0.08 | 16.07±0.03 | 14.11±0.56 | 0.088 |
| 1971 | 16.70±0.02 | 15.30±0.02 | 12.54±0.28 | 16.64±0.02 | 15.25±0.02 | — | 0.042 |
| 2131 | 16.73±0.05 | 15.52±0.06 | 13.01±0.38 | 16.70±0.06 | 15.48±0.06 | 12.91±0.40 | 0.167 |
| 2135 | 17.60±0.03 | 16.40±0.03 | 13.82±0.32 | 17.57±0.04 | 16.36±0.04 | — | 0.118 |
| 2217 | 15.77±0.27 | 13.75±0.26 | 9.86±1.40 | 15.74±0.28 | 13.72±0.26 | — | 0.294 |
| 2264 | 16.89±0.24 | 15.50±0.20 | 12.26±0.35 | — | — | 12.27±0.21 | 0.225 |
| 2292 | 17.73±0.15 | 16.78±0.16 | 14.16±1.13 | 17.58±0.17 | 16.71±0.16 | — | 0.100 |
| 2367 | 17.90±0.02 | 17.02±0.03 | 14.90±0.22 | 17.84±0.02 | 16.96±0.03 | 15.02±0.16 | 0.067 |
| 2369 | 17.71±0.03 | 16.76±0.02 | 14.70±0.20 | 17.67±0.04 | 16.72±0.03 | 14.81±0.15 | 0.068 |
| 2548 | 17.34±0.08 | 16.26±0.06 | 13.97±0.15 | 17.29±0.10 | 16.21±0.07 | 14.06±0.12 | 0.089 |
| 2558 | 16.70±0.02 | 15.73±0.02 | 13.58±0.16 | 16.68±0.02 | 15.70±0.02 | 13.61±0.12 | 0.039 |
| E1371 | 17.96±0.15 | 16.17±0.15 | 12.59±0.14 | 17.94±0.16 | 16.13±0.16 | 12.57±0.15 | 0.247 |
| E1404 | 17.82±0.06 | 16.63±0.06 | 14.08±0.14 | 17.79±0.07 | 16.59±0.07 | 14.07±0.14 | 0.169 |
| E1440 | 17.84±0.06 | 16.70±0.06 | 14.30±0.32 | 17.78±0.06 | 16.65±0.07 | 14.35±0.22 | 0.146 |
| E1447 | 18.62±0.02 | 16.93±0.02 | 13.63±0.08 | 18.59±0.03 | 16.89±0.02 | 13.59±0.10 | 0.057 |
| E1498 | 17.71±0.02 | 16.31±0.02 | 13.36±0.08 | 17.69±0.02 | 16.28±0.02 | 13.35±0.08 | 0.035 |
| E1619 | 17.75±0.02 | 16.05±0.02 | 12.70±0.08 | 17.72±0.02 | 16.00±0.03 | 12.66±0.09 | 0.043 |
| E1623 | 18.24±0.04 | 16.88±0.03 | 13.73±0.08 | 18.17±0.05 | 16.83±0.03 | 13.67±0.10 | 0.045 |

10. Figure Captions

Fig. 1.— The distribution of morphological T-types (upper) and surface brightness classes (lower) for our subsample of the FGC (shaded histogram) and the entire FGC (dotted line, scaled vertically to fit the display). The morphological classes and surface brightness classes are those listed in the FGC. The surface brightness classes are defined such that "I" is the highest surface brightness and "IV" is the lowest. We have made no correction for the slightly different surface brightness limits of the FGC and FGCE.

Fig. 2.— The distribution of blue axial ratios for our subsample of the FGC (shaded histogram) and the entire FGC (dotted line, scaled vertically to fit the display). We have made no correction for the slightly different depths of the FGC and FGCE.

Fig. 3.— B (lower left), R (upper), and K_s (lower right) images and contour diagrams of the 49 galaxies of our sample. All images are displayed with the same stretch and display range, such that apparent surface brightness variations from galaxy-to-galaxy reflect true variations in the surface brightness. The contour levels are separated by 1 mag/arcsec^2 , with the dark reference contour drawn at $\mu_B = 27.0 \text{ mag/arcsec}^2$, $\mu_R = 26 \text{ mag/arcsec}^2$, and $\mu_{K_s} = 21 \text{ mag/arcsec}^2$ in the lower left, upper, and lower right contour images respectively. The solid circle in the upper right of each image has a diameter equal to the FWHM of the point-spread function for that image. The horizontal line in the lower left of the upper R -band image is equal to $1 h_{50}^{-1} \text{ kpc}$ if the galaxy is at a distance of V_{\odot}/H_0 ; we have taken the recessional velocity V_{\odot} from the published single dish HI measurements described in §2 (if available) or from our long slit H α spectroscopy. At isophotal levels where there is sufficient signal-to-noise, contours are defined from the unsmoothed image. However, fainter isophote are defined using a smoothed version of the image (see §7). Tick marks are given at every 5 arcseconds. The light grey shading under the contours indicates regions which were masked. **THESE IMAGES ARE AVAILABLE IN POSTSCRIPT FORMAT AT <ftp://ftp.astro.washington.edu/pub/users/jd/FGC/dalcanton.f3.ps.gz> or in low-resolution JPEG format from astro-ph**

Fig. 4.— The standard deviation of unmasked sky pixels in the final B (heavy line), R (medium line) and K_s (light line, plotted as $\mu + 5$) images, as a function of the boxcar smoothing length. The dashed line gives the expected relation for a perfectly flat, uniform, Poisson sky background. Only points where there are at least 25 independent, unmasked regions in the smoothed images are plotted.

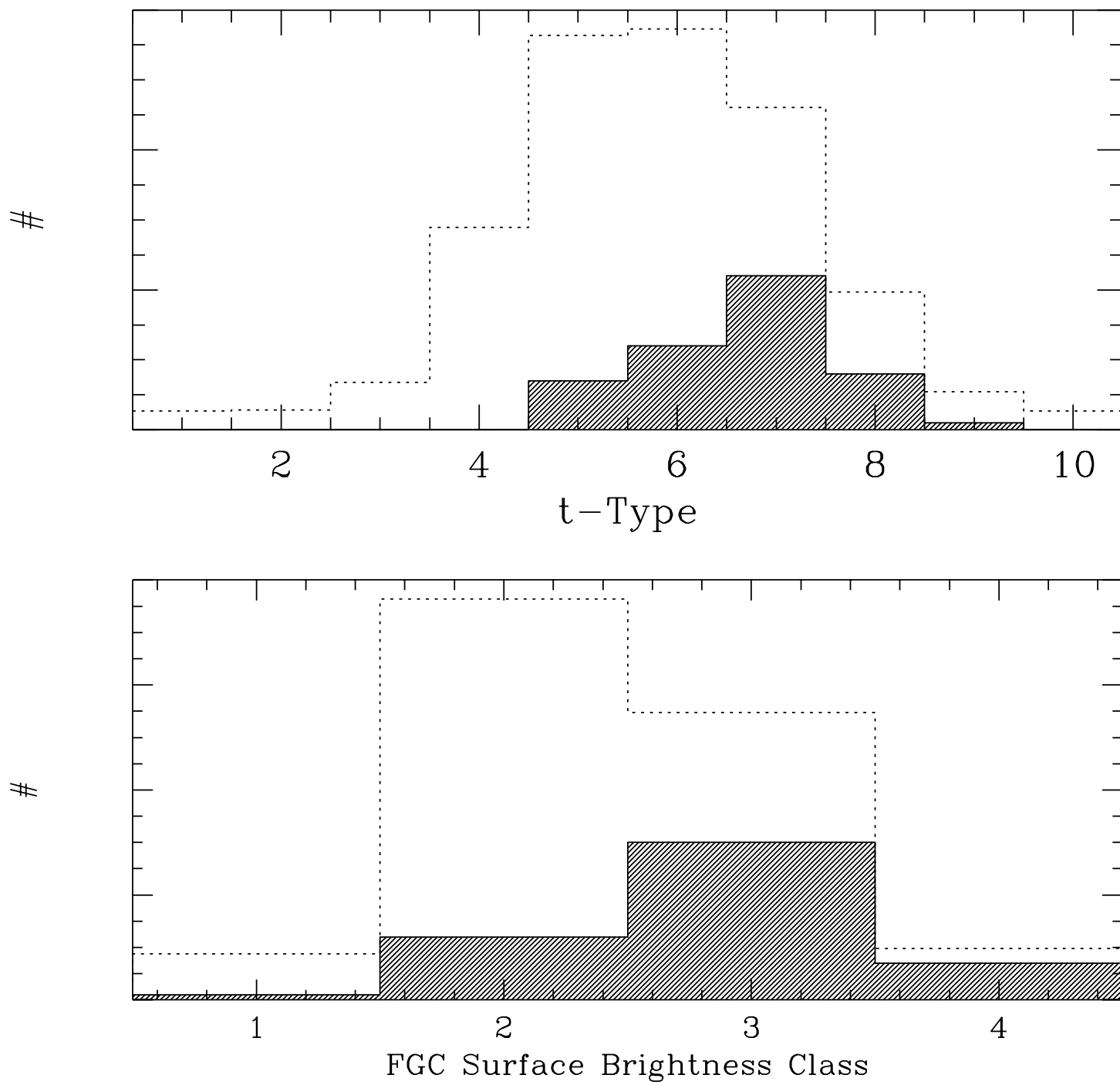


FIGURE 1

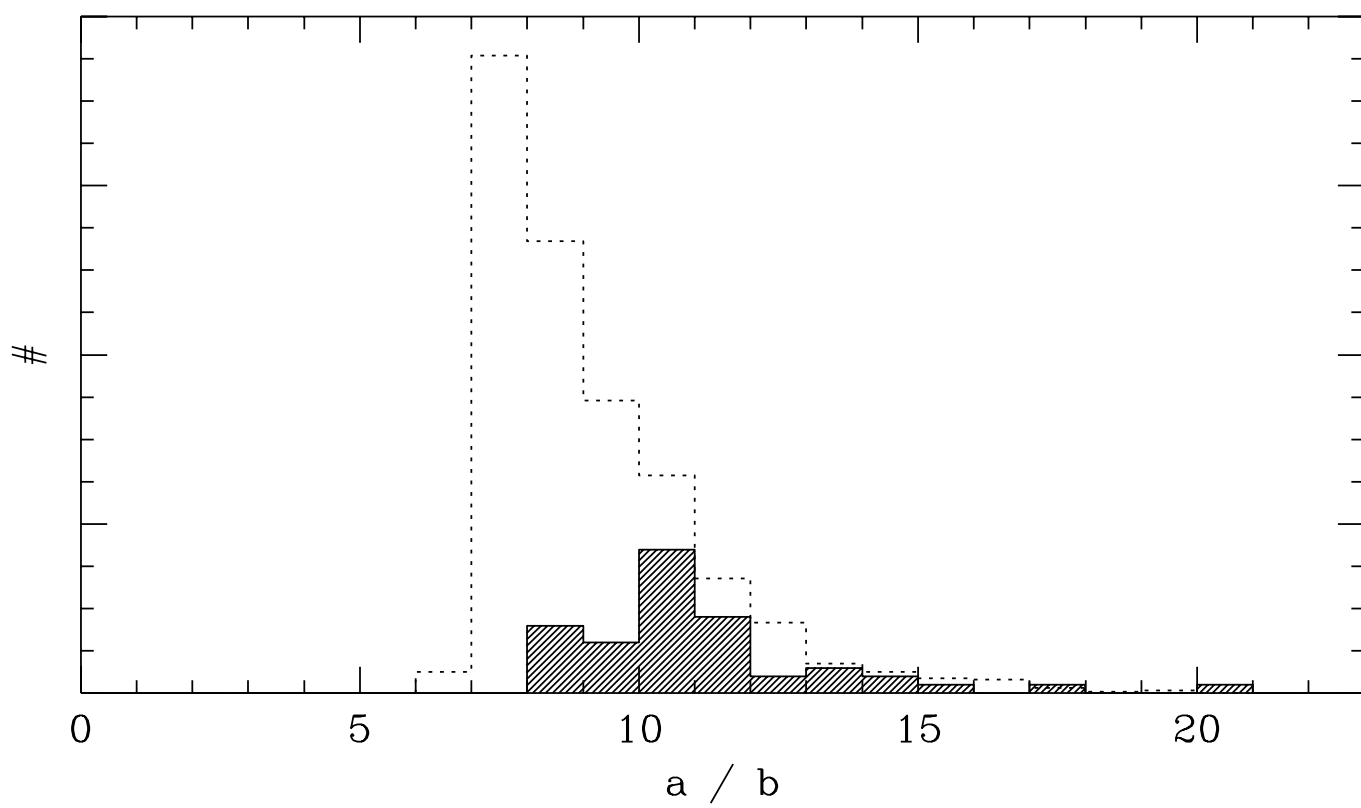


FIGURE 2

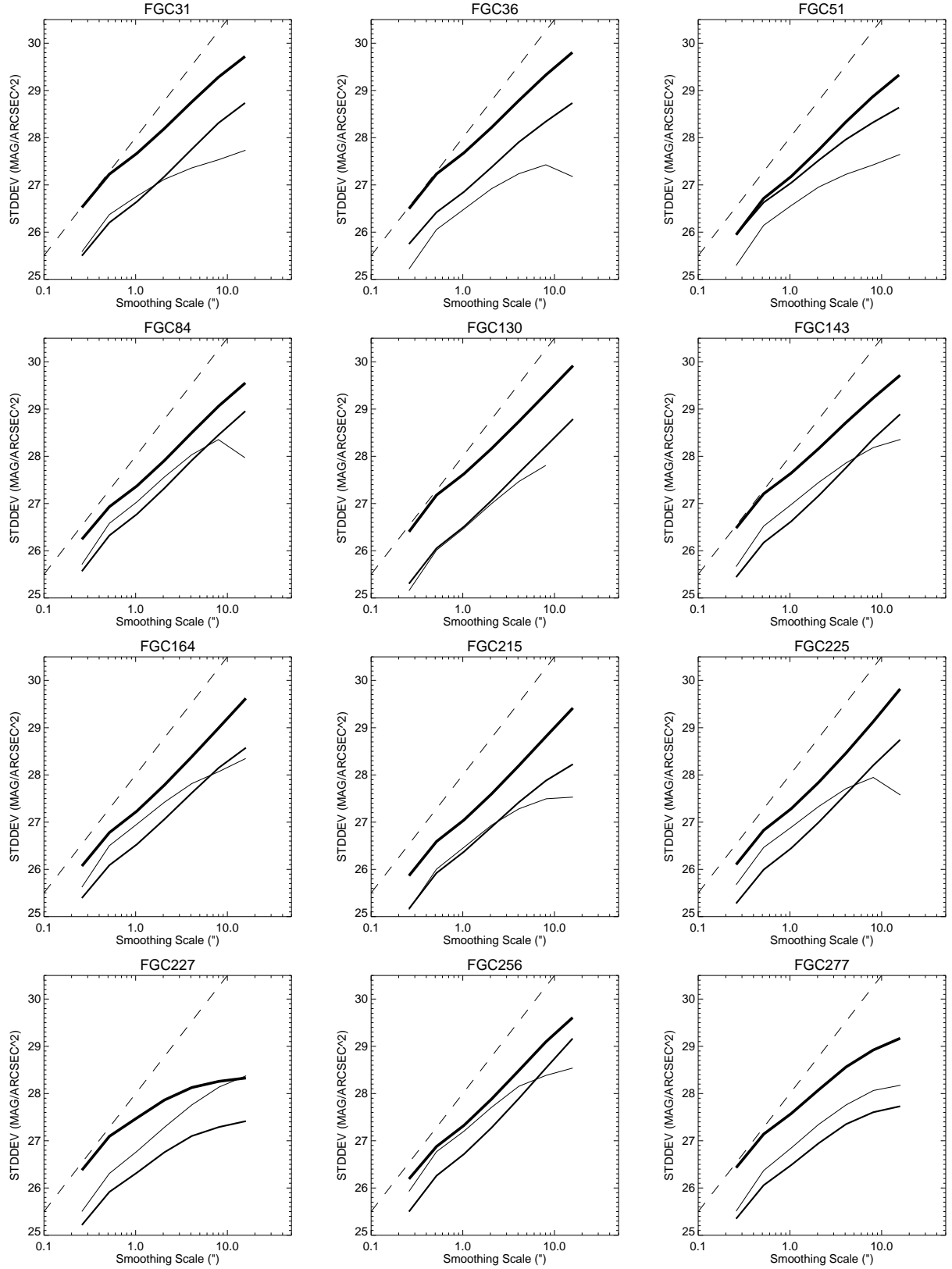


FIGURE 4

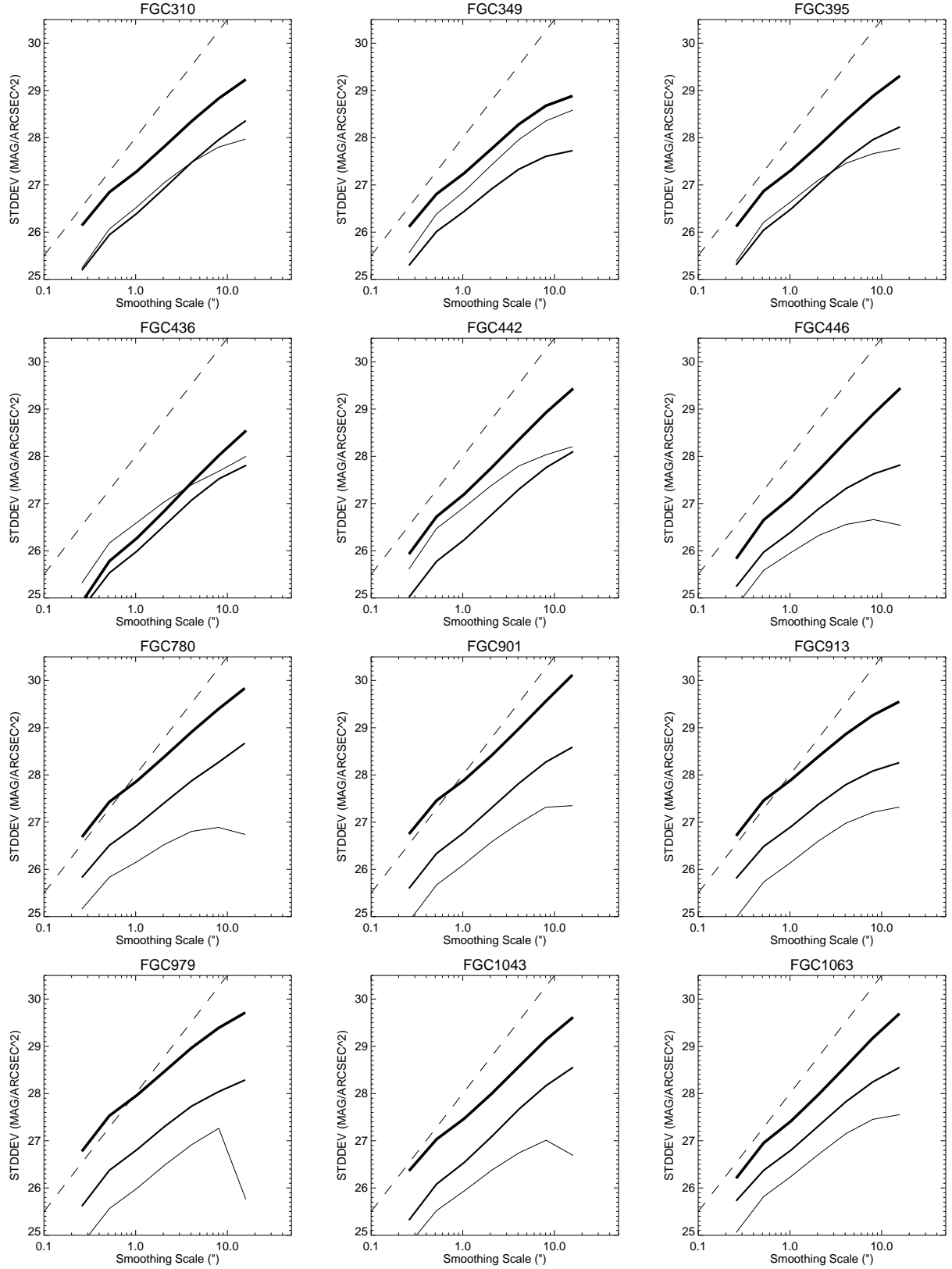


FIGURE 4 (CONTINUED)

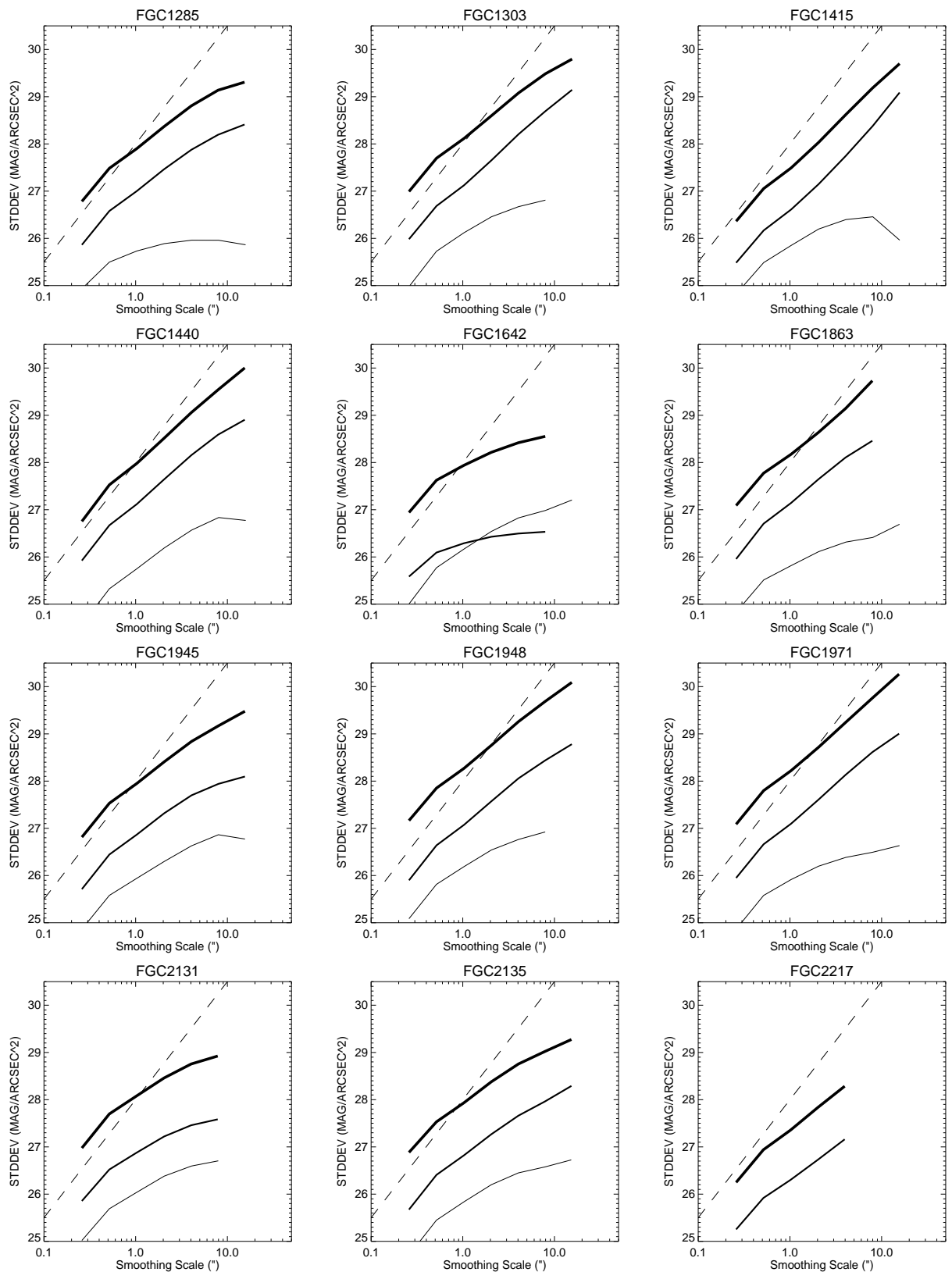


FIGURE 4 (CONTINUED)

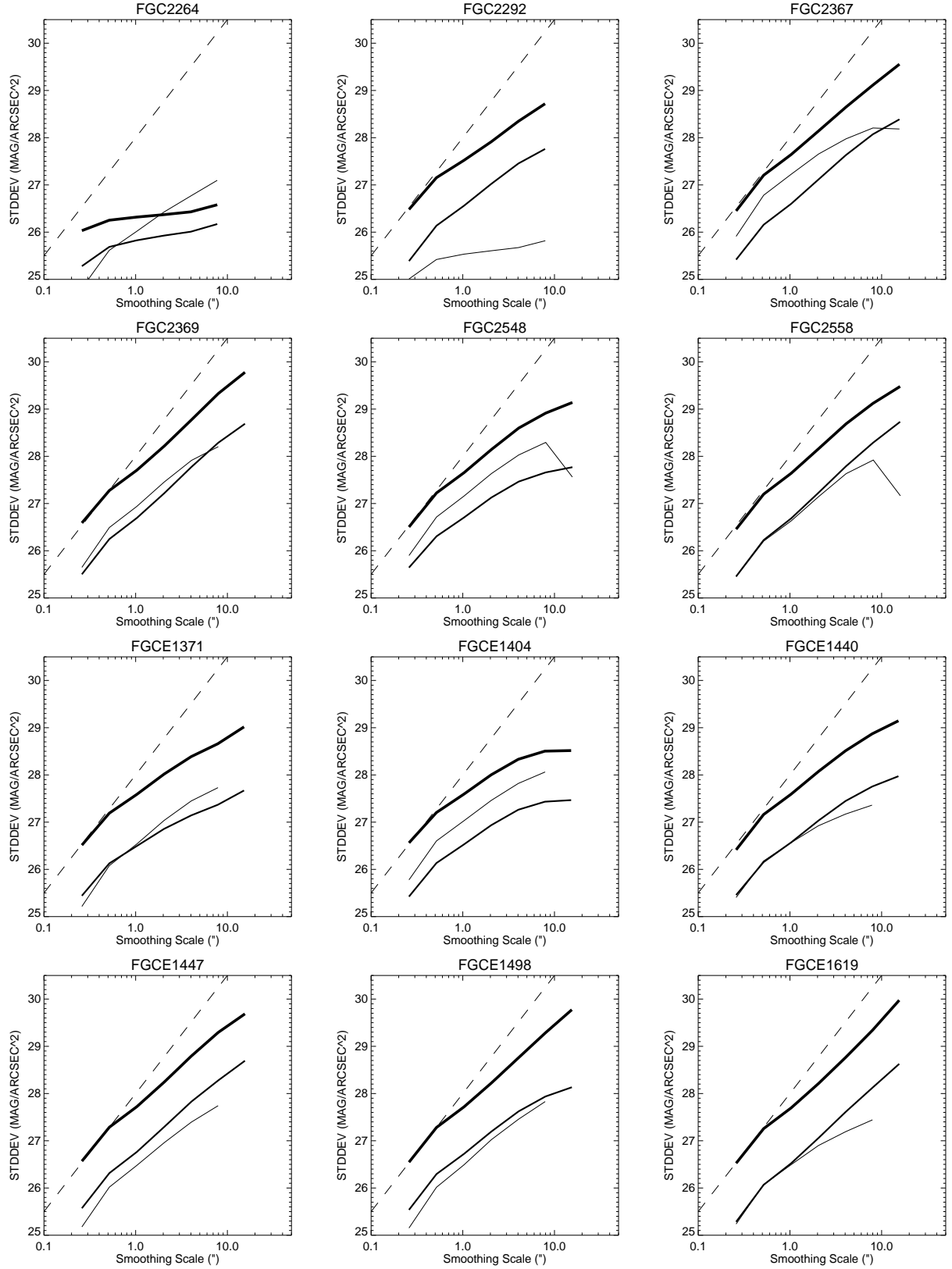


FIGURE 4 (CONTINUED)

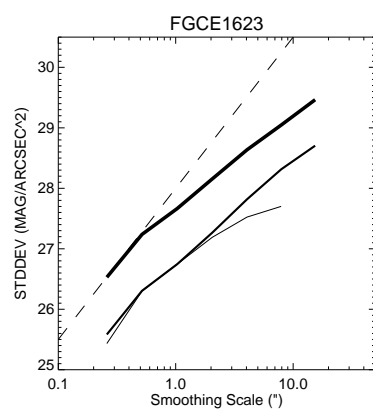


FIGURE 4 (CONTINUED)

This figure "dalcanton.f3a.jpg" is available in "jpg" format from:

<http://arxiv.org/ps/astro-ph/0005327v1>

This figure "dalcanton.f3aa.jpg" is available in "jpg" format from:

<http://arxiv.org/ps/astro-ph/0005327v1>

This figure "dalcanton.f3b.jpg" is available in "jpg" format from:

<http://arxiv.org/ps/astro-ph/0005327v1>

This figure "dalcanton.f3bb.jpg" is available in "jpg" format from:

<http://arxiv.org/ps/astro-ph/0005327v1>

This figure "dalcanton.f3c.jpg" is available in "jpg" format from:

<http://arxiv.org/ps/astro-ph/0005327v1>

This figure "dalcanton.f3cc.jpg" is available in "jpg" format from:

<http://arxiv.org/ps/astro-ph/0005327v1>

This figure "dalcanton.f3d.jpg" is available in "jpg" format from:

<http://arxiv.org/ps/astro-ph/0005327v1>

This figure "dalcanton.f3dd.jpg" is available in "jpg" format from:

<http://arxiv.org/ps/astro-ph/0005327v1>

This figure "dalcanton.f3e.jpg" is available in "jpg" format from:

<http://arxiv.org/ps/astro-ph/0005327v1>

This figure "dalcanton.f3ee.jpg" is available in "jpg" format from:

<http://arxiv.org/ps/astro-ph/0005327v1>

This figure "dalcanton.f3f.jpg" is available in "jpg" format from:

<http://arxiv.org/ps/astro-ph/0005327v1>

This figure "dalcanton.f3ff.jpg" is available in "jpg" format from:

<http://arxiv.org/ps/astro-ph/0005327v1>

This figure "dalcanton.f3g.jpg" is available in "jpg" format from:

<http://arxiv.org/ps/astro-ph/0005327v1>

This figure "dalcanton.f3gg.jpg" is available in "jpg" format from:

<http://arxiv.org/ps/astro-ph/0005327v1>

This figure "dalcanton.f3h.jpg" is available in "jpg" format from:

<http://arxiv.org/ps/astro-ph/0005327v1>

This figure "dalcanton.f3hh.jpg" is available in "jpg" format from:

<http://arxiv.org/ps/astro-ph/0005327v1>

This figure "dalcanton.f3i.jpg" is available in "jpg" format from:

<http://arxiv.org/ps/astro-ph/0005327v1>

This figure "dalcanton.f3ii.jpg" is available in "jpg" format from:

<http://arxiv.org/ps/astro-ph/0005327v1>

This figure "dalcanton.f3j.jpg" is available in "jpg" format from:

<http://arxiv.org/ps/astro-ph/0005327v1>

This figure "dalcanton.f3jj.jpg" is available in "jpg" format from:

<http://arxiv.org/ps/astro-ph/0005327v1>

This figure "dalcanton.f3k.jpg" is available in "jpg" format from:

<http://arxiv.org/ps/astro-ph/0005327v1>

This figure "dalcanton.f3kk.jpg" is available in "jpg" format from:

<http://arxiv.org/ps/astro-ph/0005327v1>

This figure "dalcanton.f3l.jpg" is available in "jpg" format from:

<http://arxiv.org/ps/astro-ph/0005327v1>

This figure "dalcanton.f3ll.jpg" is available in "jpg" format from:

<http://arxiv.org/ps/astro-ph/0005327v1>

This figure "dalcanton.f3m.jpg" is available in "jpg" format from:

<http://arxiv.org/ps/astro-ph/0005327v1>

This figure "dalcanton.f3mm.jpg" is available in "jpg" format from:

<http://arxiv.org/ps/astro-ph/0005327v1>

This figure "dalcanton.f3n.jpg" is available in "jpg" format from:

<http://arxiv.org/ps/astro-ph/0005327v1>

This figure "dalcanton.f3nn.jpg" is available in "jpg" format from:

<http://arxiv.org/ps/astro-ph/0005327v1>

This figure "dalcanton.f3o.jpg" is available in "jpg" format from:

<http://arxiv.org/ps/astro-ph/0005327v1>

This figure "dalcanton.f3oo.jpg" is available in "jpg" format from:

<http://arxiv.org/ps/astro-ph/0005327v1>

This figure "dalcanton.f3p.jpg" is available in "jpg" format from:

<http://arxiv.org/ps/astro-ph/0005327v1>

This figure "dalcanton.f3pp.jpg" is available in "jpg" format from:

<http://arxiv.org/ps/astro-ph/0005327v1>

This figure "dalcanton.f3q.jpg" is available in "jpg" format from:

<http://arxiv.org/ps/astro-ph/0005327v1>

This figure "dalcanton.f3qq.jpg" is available in "jpg" format from:

<http://arxiv.org/ps/astro-ph/0005327v1>

This figure "dalcanton.f3r.jpg" is available in "jpg" format from:

<http://arxiv.org/ps/astro-ph/0005327v1>

This figure "dalcanton.f3rr.jpg" is available in "jpg" format from:

<http://arxiv.org/ps/astro-ph/0005327v1>

This figure "dalcanton.f3s.jpg" is available in "jpg" format from:

<http://arxiv.org/ps/astro-ph/0005327v1>

This figure "dalcanton.f3ss.jpg" is available in "jpg" format from:

<http://arxiv.org/ps/astro-ph/0005327v1>

This figure "dalcanton.f3t.jpg" is available in "jpg" format from:

<http://arxiv.org/ps/astro-ph/0005327v1>

This figure "dalcanton.f3tt.jpg" is available in "jpg" format from:

<http://arxiv.org/ps/astro-ph/0005327v1>

This figure "dalcanton.f3u.jpg" is available in "jpg" format from:

<http://arxiv.org/ps/astro-ph/0005327v1>

This figure "dalcanton.f3uu.jpg" is available in "jpg" format from:

<http://arxiv.org/ps/astro-ph/0005327v1>

This figure "dalcanton.f3v.jpg" is available in "jpg" format from:

<http://arxiv.org/ps/astro-ph/0005327v1>

This figure "dalcanton.f3vv.jpg" is available in "jpg" format from:

<http://arxiv.org/ps/astro-ph/0005327v1>

This figure "dalcanton.f3w.jpg" is available in "jpg" format from:

<http://arxiv.org/ps/astro-ph/0005327v1>

This figure "dalcanton.f3ww.jpg" is available in "jpg" format from:

<http://arxiv.org/ps/astro-ph/0005327v1>

This figure "dalcanton.f3x.jpg" is available in "jpg" format from:

<http://arxiv.org/ps/astro-ph/0005327v1>

This figure "dalcanton.f3y.jpg" is available in "jpg" format from:

<http://arxiv.org/ps/astro-ph/0005327v1>

This figure "dalcanton.f3z.jpg" is available in "jpg" format from:

<http://arxiv.org/ps/astro-ph/0005327v1>